LITHOS 420–421 (2022) 106700

Contents lists available at ScienceDirect

LITHOS

journal homepage: www.elsevier.com/locate/lithos

Petrogenesis and tectonic implication of Neoproterozoic I-Type Granitoids and orthogneisses in the Goa-Mandja area, Central African Fold Belt (Cameroon)

Bovari Syprien Yomeun [a,b], Wei Wang [a,*], Jean Pierre Tchouankoue [b], Michele Sandra Kamguia Kamani [a,b], Kevin Igor Azeuda Ndonfack [b,c], Si-Fang Huang [a], Emmanuel Archelaus Afanga Basua [a,b], Gui-Mei Lu [a], Er-Kun Xue [a]

[a] State Key Laboratory of Geological Processes and Mineral Resources, School of Earth Sciences, China University of Geosciences, Wuhan 430074, China
[b] Department of Earth Sciences, University of Yaoundé I, P.O. Box 812, Yaoundé, Cameroon
[c] School of Civil and Environmental Engineering, University of Science and Technology Beijing, Beijing 100083, PR China

ARTICLE INFO

Keywords:
Pan-African magmatism
Goa-Mandja I-type granitoids
Petrogenesis
Central African Fold Belt

ABSTRACT

The geological evolution of the Central African Fold Belt (CAFB) remains debated. The granitoids, orthogneisses and granitic veins from the Goa-Mandja area (Adamawa-Yade domain) are considered to constrain this belt. These rocks are consistent with late-D_2 regional emplacement and synchronous with the magmatism at ~600 Ma within the CAFB in Cameroon and its extension into northeastern Brazil, as the zircon U—Pb dating points to 603–598 Ma crystallization ages. Analytical data reveal slightly elevated $\delta^{18}O_{zrn}$ (6.45–7.17‰) and $\delta^{18}O_{WR}$ (8.20–8.61‰), moderate to high SiO_2 (59.70–77.23 wt%), low MgO (0.07–2.77 wt%), Cr (0.29–55.12 ppm), Ni (0.45–33.6 ppm), V (1.52–116.62 ppm) and $Mg^{\#}$ (0.02–0.36) contents, indicating crustal origin. The low to medium $^{87}Sr/^{86}Sr_i$ (0.703328–0.722670) and positive to negative $\varepsilon_{Nd(t)}$ (+5.7 to −9.9), coupled with the diversity of Nd model ages (T_{DM2}) support the heterogeneity of crustal protoliths. The high positive $\varepsilon_{Nd(t)}$ (+5.7) of the granitic vein indicates derivation from juvenile Neoproterozoic (Nd-T_{DM2} at 854 Ma) crustal protolith. $T_{DM2(Nd)}$ and $T_{DM2(Hf)}$ ages of 1188–2120 Ma and 2173–2480 Ma also suggest the involvement of Mesoproterozoic to Paleoproterozoic crustal protoliths.

Samples show metaluminous to weakly peraluminous, high-K calc-alkaline to shoshonitic and I-type granitoid features and are similar with crustal rocks in regard to LILE (Rb, K) and LREE enrichments and HFSE (Nb, Ta, Ti) depletions. These combined features indicate slab subduction related setting for the magma generation. Slab subduction may have generated the heat necessary to provoke partial melting at the lower crustal level. Considering their position close to the Tchollire-Banyo Fault corridor, at the transition between the Adamawa-Yade and northern domains, the subduction derived features shown by the Goa-Mandja I-type granitoids could be related to the subduction of an old plate boundary during amalgamation of Gondwana. Therefore, the Goa-Mandja area records dominant magmatic accretion along the northern margin of the Congo craton (active margin) associated with a possible northwestern subduction.

1. Introduction

The Central African Fold Belt (CAFB) was formed by the convergence of the Congo and West-African cratons with the Saharan Metacraton during amalgamation of the Gondwana supercontinent (Abdelsalam et al., 2002; Ngako et al., 2008; Shellnutt et al., 2019; Toteu et al., 2004) (Fig. 1a), leading to the complexity of the geodynamic setting. It is limited to the south, north, west and east, respectively, by the Congo Craton, the Saharan Metacraton, the coeval Trans-Saharan orogenic belt (Abdelsalam et al., 2002; Kröner and Stern, 2004; Shellnutt, 2021) and the East African belt. This belt underlies the east of Nigeria, Cameroon, the south of Chad and Central African Republic (Fig. 1b) and extends into Neoproterozoic Brasiliano belt exposed in the Borborema Province, northeast Brazil (e.g., Lerouge et al., 2006; Van Schmus et al., 2008)

* Corresponding author.
E-mail address: wwz@cug.edu.cn (W. Wang).

https://doi.org/10.1016/j.lithos.2022.106700
Received 31 October 2021; Received in revised form 6 April 2022; Accepted 8 April 2022
Available online 14 April 2022

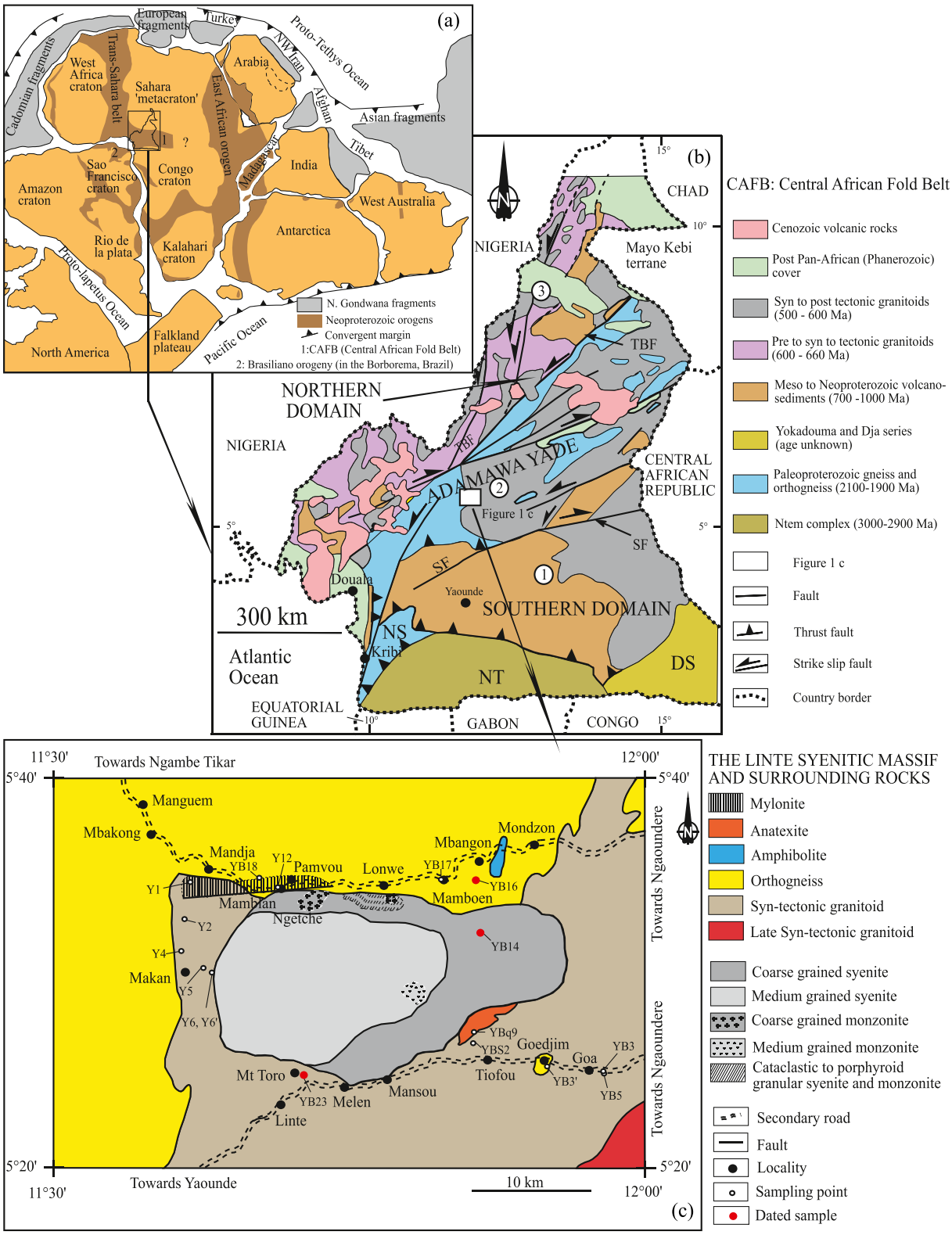

Fig. 1. (a) Schematic reconstitution of the Gondwana supercontinent at ca. 540 Ma (adapted after Kusky et al., 2003; Kröner and Stern, 2004; Wang et al., 2019 and references therein). (b) Geological map of Cameroon showing the major lithotectonic domains (compiled from Kwékam et al., 2010 and Van Schmus et al., 2008). SF (Sanaga fault), TBF (Tchollire-Banyo fault), NT (Ntem complex), DS (Dja group), NS (Nyong group), 1 = Yaounde domain, 2 = Adamawa-Yade domain, 3 = northern domain. (c) Study area modified from Weecksteen (1957).

Table 1
Codes, locations (GPS), textures, estimated modal compositions (vol%), rock types (using the QAP diagram) and analyzed methods of granitoids and orthogneisses from the Goa-Mandja area.

Sample code	Sampling site (GPS)	Texture	Estimated modal composition (vol %)	Sample code	Sampling site (GPS)	Rock name (QAP diagram)	Analyzed methods
Y1	N 05°34′41.3” E 011°37′01.7”	Protomylonitic to cataclastic heterogranular	Or: 15, Mc: 25, Pl: 27, Qtz: 3, Hbl: 15, Bt: 10, Op: 2, Ttn: 1, Zrn: 1, and Ap: 1	Y1	N 05°34′41.3” E 011°37′01.7”	Monzonite	Whole-rock major and trace elements geochemistry and whole rock Sr—Nd isotopic
Y4	N 05°31′10.7” E 011°36′34.7”	Granular to porphyroid granular	Or: 20, Mc: 15, Pl: 30, Qtz: 15, Hbl: 5, Bt: 10, Op: 2, Ttn: 1 Zrn: 1 and Ap: 1	Y4	N 05°31′10.7” E 011°36′34.7”	Quartz Monzonite	Whole-rock major and trace elements geochemistry and whole rock Sr—Nd isotopic
Y6 and Y6’	N 05°30′03.6” E 011°38′10.1”	Granular to porphyroid granular	Or:25, Mc: 15, Pl: 30, Qtz: 10, Hbl: 10, Bt: 5, Op: 2, Ttn: 1, Zrn: 1 and Ap: 1	Y6 and Y6’	N 05°30′03.6” E 011°38′10.1”	Quartz Monzonite	Whole-rock major and trace (except YB6’) elements geochemistry
YB23	N 05°24′47.9” E 011°42′50.4”	Granular to porphyroid granular with sub-oriented tendence	Or: 25, Mc: 15, Pl: 25, Qtz: 15, Hbl: 5, Bt: 10, Op: 2, Ttn: 1, Zrn: 1 and Ap: 1	YB23	N 05°24′47.9” E 011°42′50.4”	Quartz Monzonite	Whole-rock major and trace elements geochemistry, whole rock Sr—Nd isotopic and zircon U-Pb-Hf-O isotopic
YBS2	N 05°26′24” E 011°51′44.17”	Granular to porphyroid granular	Or: 15, Mc: 20, Pl: 35 Qtz: 15 Hbl: 5, Bt: 5, Op: 2, Ttn: 1, Zrn: 1 and Ap: 1	YBS2	N 05°26′24” E 011°51′44.17”	Quartz Monzonite	Whole-rock major and trace elements geochemistry
YBqf	N 05°26′59.9” E 011°51′25.4”	Granular to porphyroid granular with sub-oriented tendence	Or:25, Mc: 15, Qtz: 15, Pl: 30, Hbl: 3, Bt: 7, Op: 2, Ttn: 1, Zrn: 1 and Ap: 1	YBqf	N 05°26′59.9” E 011°51′25.4”	Quartz Monzonite	Whole-rock major and trace elements geochemistry and whole rock Sr—Nd isotopic
YB14	N 05°32′04.7” E 011°51′44.2”	Granular to suboriented granular	Or: 5, Mc: 20, Pl: 35, Qtz: 35, Hbl: 5, Bt: 2, Op: 1, Ttn: 1, Zrn: 1	YB14	N 05°32′04.7” E 011°51′44.2”	Granite	Whole-rock major and trace elements geochemistry, whole rock Sr—Nd isotopic and zircon U-Pb-Hf-O isotopic
Y2	N 05°32′48.3” E 011°36′46.2”	Porphyroid granular with sub-oriented tendence	Or: 15, Mc: 25, Qtz: 30, Pl: 10, Hbl: 5, Bt: 10, Op: 2, Ttn: 1, Zrn: 1 and Ap: 1	Y2	N 05°32′48.3” E 011°36′46.2”	Granite	Whole-rock major and trace elements geochemistry
YB3	N 05°24′59.2” E 011°57′57.0”	Granular	Or: 20, Mc: 15, Pl: 10, Qtz: 25, Hbl: 10, Bt: 15, Op: 3, Ttn: 1, Zrn: 1 and Ap: 1	YB3	N 05°24′59.2” E 011°57′57.0”	Granite	Whole-rock major and trace elements geochemistry and whole rock Sr—Nd isotopic
YB5	N 05°24′54.4” E 011°57′57.8”	granular to porphyroid granular	Or: 25, Mc: 20, Qtz: 25, Pl: 10, Hbl: 5, Bt: 10, Op: 3, Ttn: 1, Zrn: 1 and Ap: 1	YB5	N 05°24′54.4” E 011°57′57.8”	Granite	Whole-rock major and trace elements geochemistry and whole rock Sr—Nd isotopic

(*continued on next page*)

Table 1 (*continued*)

Sample code	Sampling site (GPS)	Texture	Estimated modal composition (vol %)	Sample code	Sampling site (GPS)	Rock name (QAP diagram)	Analyzed methods
Y5	N 05°30′18.6” E 011°37′43.1”	granular to porphyroid granular	Or: 25, Mc: 30, Pl: 10, Qtz: 20 Hbl: 5, Bt: 5, Op: 2, Ttn: 1, Zrn: 1 and Ap: 1	Y5	N 05°30′18.6” E 011°37′43.1”	Granite	Whole-rock major and trace elements geochemistry
YB16	N 05°34′46.6” E 011°51′29.4”	heterogranoblastic	Or: 5, Mc: 15, Pl: 40, Qtz: 20, Hbl: 15, Bt: 5, Op: 2, Ttn: 1, Zrn: 1 and Ap: 1	YB16	N 05°34′46.6” E 011°51′29.4”	Granodiorite	Whole-rock major and trace elements geochemistry, whole rock Sr—Nd isotopic and zircon U-Pb-Hf-O isotopic
YB17	N 05°34′49.4” E 011°49′43.8”	Granoblastic	Or: 25, Mc: 15, Pl: 30, Qtz: 15, Hbl: 15, Bt: 5, Op: 2, Ttn: 1, Zrn: 1 and Ap: 1	YB17	N 05°34′49.4” E 011°49′43.8”	Quartz Monzonite	Whole-rock major and trace elements geochemistry and whole rock Sr—Nd isotopic
YB18	N 05°34′55.3” E 011°40′32.3”	Granoblastic	Or: 30, Mc: 15, Pl: 10, Qtz: 35, Hbl: 2, Bt: 5, Op: 1, Ttn, Zrn and Ap: 2	YB18	N 05°34′55.3” E 011°40′32.3”	Granite	Whole-rock major and trace elements geochemistry and whole rock Sr—Nd isotopic
YB3’	N 05°25′13.5” E 011°55′10.5”	Granoblastic	Or: 15, Mc: 10, Pl: 10, Qtz: 35, Hbl: 10, Bt: 15, Op: 3, Ttn: 1, Zrn: 1 and Ap: 1	YB3’	N 05°25′13.5” E 011°55′10.5”	Granite	Whole-rock major and trace elements geochemistry and whole rock Sr—Nd isotopic
Y12	N 05°34′24.6” E 011°41′28.7”	Granoblastic	Or: 20, Mc: 15, Pl: 25, Qtz: 10 Hbl: 10, Bt: 15, Op: 2, Ttn: 1, Zrn: 1 and Ap: 1	Y12	N 05°34′24.6” E 011°41′28.7”	Quartz Monzonite	Whole-rock major and trace elements geochemistry and whole rock Sr—Nd isotopic

(Fig. 1a). In Cameroon, the CAFB generated low- to high-grade metamorphic and magmatic complexes that were subdivided by major crustal strike-slip shear zones into three geodynamic domains (e.g., Tchakounté et al., 2017; Toteu et al., 2004; Van Schmus et al., 2008): (1) the old continental domain or southern domain, (2) the intermediate continental domain or central domain also called Adamawa-Yade domain (Toteu et al., 2004) and (3) the accretion zone or northern domain (Fig. 1b).

Orthogneisses, granitoids and plutonic massifs are common within the CAFB included within the Adamawa-Yade domain and parts of the Cameroon territory to the west of the Tchollire-Banyo Fault (TBF) (Fig. 1b). These rocks are I- and S-types showing high-K calc-alkaline to shoshonitic affinities (e.g., Djouka-Fonkwé et al., 2008; Kamguia Kamani et al., 2021; Kwékam et al., 2020a, 2020b; Ngamy Kamwa et al., 2019; Ngo Belnoun et al., 2013; Tchakounté et al., 2021; Tchameni et al., 2006; Tchouankoue et al., 2016) and were emplaced during the initial to paroxysmal phase of the Pan-African orogeny at ca. 660–580 Ma (e.g., Azeuda Ndonfack et al., 2022; Ganwa et al., 2018; Kamguia Kamani et al., 2021; Kanouo et al., 2021; Kwékam et al., 2020b; Li et al., 2017; Tchakounté et al., 2021; Tchouankoue et al., 2016). However, researchers suggested that the emplacement in western Cameroon would have ended at ca. 565–545 Ma (e.g., Kwékam et al., 2020a, 2020b; Ngo Belnoun et al., 2013). The study of these rocks and massifs gives indications on various sources and evolutions, and unveils the geodynamic environments, which are sometimes misunderstood because of the lack of systematic geochemical, geochronological and isotopic data. The Goa-Mandja area, located at the vicinity of the TBF corridor at the transition between the Adamawa-Yade and northern domains (Fig. 1b), and composed of large surfaces of migmatites (orthogneisses) and *syn*-tectonic granitoids surrounding the syenitic massif of Linte (Weecksteen, 1957), is best to characterize the tectonic evolution of this portion of CAFB. Therefore, this area was chosen for detailed petrological, geochemical, isotopic and geochronological studies in order to elucidate the nature, timing, and emplacement conditions, and also to enlarge the understanding of the geodynamic evolution of the CAFB. The present contribution is focused on zircon U—Pb geochronology, whole-rock major and trace elements geochemistry, whole-rock Nd—Sr and zircon O and Lu—Hf isotopes. This will enhance discussions on the petrogenesis and geodynamic implications of the Goa-Mandja area.

2. Geological setting

The Adamawa-Yade domain is a large and complex heterogeneous domain, which could be interpreted as a micro-continent, rifted away from the Congo Craton during the early Neoproterozoic (Tchakounté et al., 2017). It is limited to the north by the TBF and to the south by the Sanaga Fault (SF) (Fig. 1b). The Adamawa-Yade domain consists of widespread rejuvenated syn- to late-tectonic magmatic rocks (granitoids) of high-K calk-alkaline to shoshonitic affinities (Ganwa et al., 2011; Tchameni et al., 2006), mainly characterized by Paleoproterozoic to Archean inheritances (e.g., Ganwa et al., 2016). Contrary to the

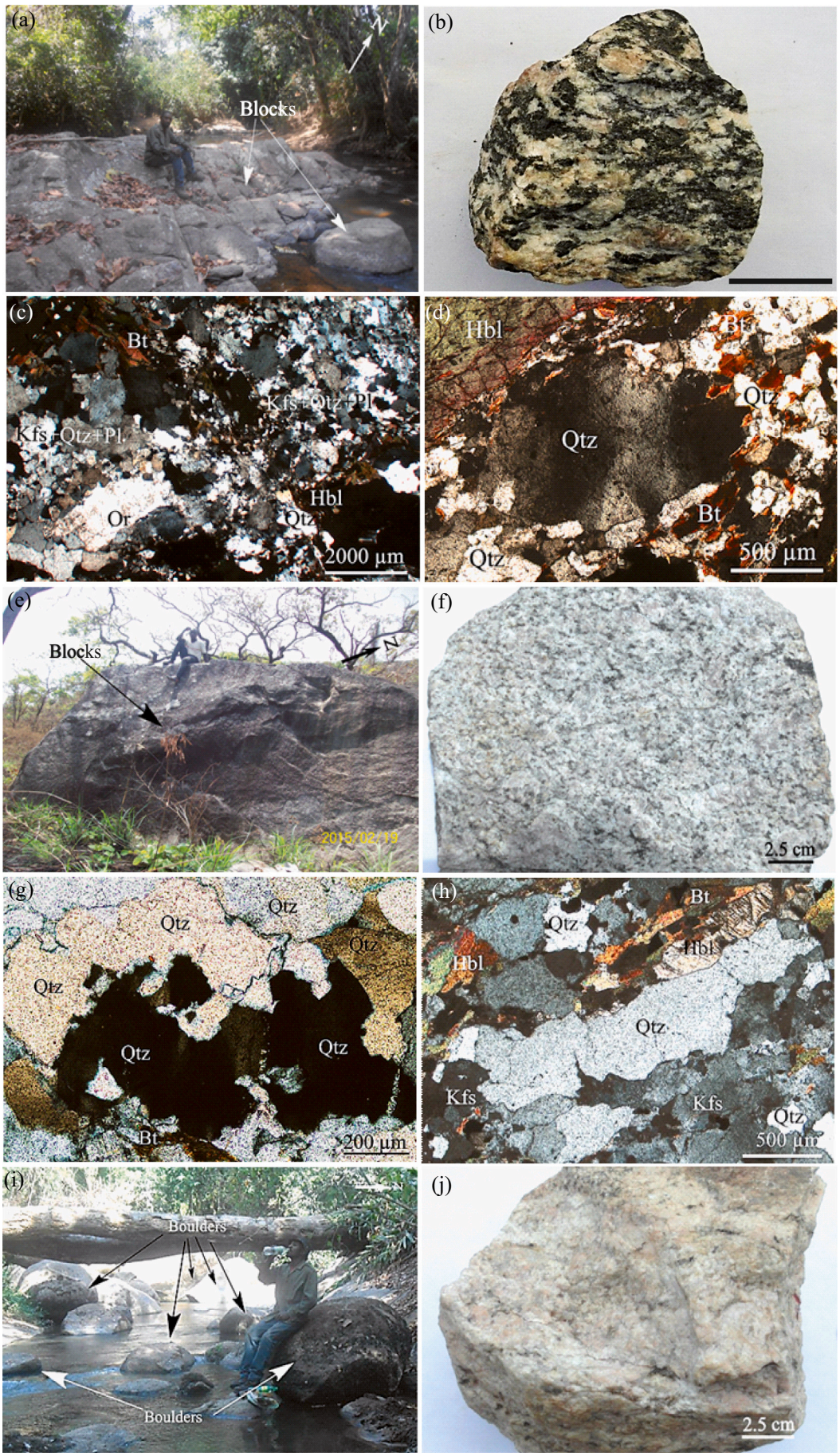

(caption on next page)

Fig. 2. Selected outcrops, hand samples and microphotographs of granitoids from the Goa-Mandja area (c, d, g and h under crossed polarized light). (a) Outcrops of monzonite in the shape of blocks. (b) Hand sample of monzonite spotted with light and dark colors and showing protomylonitic feature. Microphotographs of monzonites showing (c) crushed Qtz, Kfs and Pl crystals in a cataclastic heterogranular texture and (d) sub-ovoid phenocryst of Qtz surrounded by microcrysts in heterogranoblastic texture. (e) Outcrop of quartz monzonite in the shape of block. (f) Hand sample of quartz monzonite showing pinkish grey color and granular texture. Microphotographs of quartz monzonites showing (g) a granular texture and anhedral to amoeboid Qtz crystals and (h) flattened and oriented Qtz crystal. (i) Outcrops of granite in the shape of boulders. (j) Hand sample of granite showing pinkish color and granular texture. Abbreviations: Qtz (quartz), Or (orthoclase), Kfs (K-feldspar), Pl (plagioclase), Hbl (hornblende) and Bt (biotite).

Adamawa-Yade domain, juvenile calc-alkaline, high-K calk-alkaline to shoshonitic granitoids with Nd-T_{DM} ages not older than the Paleoproterozoic are generally found in the Northern and Western Cameroon to the west of the TBF (e.g., Dawaï et al., 2013; Djouka-Fonkwé et al., 2008; Kwékam et al., 2010, 2020a, 2020b; Tchouankoue et al., 2016). Four phases of deformation D_1 (≥620 Ma), D_2 (ca. 620–600 Ma), D_3 (ca. 590–580 Ma) and D_4 (580–560 Ma) (Li et al., 2017) are associated to these rocks in the Adamawa-Yade domain and parts of the Cameroon territory to the west of the TBF.

As mentioned above, the Goa-Mandja area is located at the proximity of the TBF corridor, between latitudes 5°20′ and 5°40′ N and longitudes 11°30′ and 12°00′ E, at about 260 km N of Yaounde (Fig. 1c). It belongs to the Adamawa-Yade domain (Fig. 1b) and is made up of granitoids and orthogneisses surrounding a syenitic batholith (Fig. 1c) also called the Linte massif (Yomeun et al., 2022).

3. Petrography

The studied rocks are mainly granitoids and orthogneisses outcropping around the Linte syenitic massif. Based on the estimated modal compositions (Table 1) plotted in the QAP diagram, granitoids are a mixture of monzonites, quartz monzonites and granites (Fig. 6a).

3.1. Monzonites

Monzonites outcrop in the shape of boulders and blocks (Fig. 2a) of centimeter to several meters and slabs of several meters. These rocks, spotted with light and dark colors (Fig. 2b), are protomylonitic (submylonitic foliation outlined by the suborientation of clasts from N135°E to 150°E) (Fig. 2b), cataclastic heterogranular (Fig. 2c) and/or heterogranoblastic in texture. They are found at the northwest of the syenitic massif. Anhedral, angular, subrounded, ovoid (Fig. 2d) or subsigmoidal, micro to megaclasts of quartz (~3%), orthoclase (~15%), microcline (~25%), plagioclase (~27%), green hornblende (~15%) and biotite (~10%) are the major minerals followed by the minor accessory minerals. Ferromagnesians are generally gathered in associations and/or clustered between quartz and feldspars. The growth of fine dust of secondary muscovite and red products lead certain plagioclases to show cloudy aspect. Some green hornblende crystals are partially transformed into biotite and/or into a reddish product. At certain places, biotite flakes are partially transformed into chlorite and/or a reddish product. Opaque minerals (~1–2%) are mostly associated to ferromagnesians. The other accessory minerals are subrounded to euhedral microcrysts of titanite (≤ 1%), apatite (≤ 1%), and zircon (≤ 1%) found as inclusions and/or isolated between quartz, feldspars and ferromagnesians.

3.2. Quartz monzonites

Quartz monzonites outcrop in the shape of boulders and blocks (Fig. 2e) of centimeter to several meters and steep hills and slabs of several tens of meters. They are pinkish grey (Fig. 2f) to pinkish and are generally/locally mixed with granites at the western, southern and eastern part of the syenitic massif. Their texture varies from granular to granular porphyroid, and sometimes show a slight preferential orientation. These rocks consist of quartz (~10–15%), plagioclase (~25–35%), orthoclase (~15–25%), microcline (~15–20%), biotite (~5–10%), green hornblende (~3–10%) partially transformed into biotite at certain places and accessory opaque minerals (≤ 2%), titanite (≤ 1%), zircon (≤ 1%) and apatite (≤ 1%). Quartz is constituted of subrounded to anhedral microcrysts haphazardly ranged or grouped as oriented monomineral assemblages. It is also found as anhedral to amoeboid (Fig. 2g) phenocrysts and scarce flattened and oriented megacrysts (Fig. 2h). Orthoclase crystals are sometimes converted into microcline. Some of these alkali feldspars (porphyrocrysts) bear numerous myrmeckitic microstructures. They are also perthitized, crackled and show cloudy aspect due to the development of fine dusts of muscovite. Reddish traces of kaolinisation are found along their cracks. Plagioclase can show deformed twinning. Their aspect is cloudy due to the sericitization and the presence of reddish products. Rocks are sporadically cataclazed, deformed and show a submylonitic texture.

3.3. Granites

Granites are mixed with monzonites and quartz monzonites at the western, eastern and at the southern part of the syenitic massif. Their outcrops are found in the shape of boulders (Fig. 2i) and slabs. They are pinkish grey to pinkish (Fig. 2j), but also reddish. Their texture is granular (Fig. 3a) to granular porphyroid and can show a suborientation. They are made up of quartz (~20–30%), orthoclase (~15–25%), microcline (~15–30%), plagioclase (~10%), green hornblende (~5–10%), and biotite (~5–15%). Accessory minerals are opaque crystals (~2–3%), titanite (≤ 1%), apatite (≤ 1%), and zircon (≤ 1%). Granites display the same petrographic description of quartz monzonites, from which they only differ by the abundance of different minerals. The reddish granites have been cataclazed. They show numerous crushed feldspars, twisted, flattened and elongated crystals of quartz and feldspars, fibrous trails of quartz similar to strain fringes (Fig. 3b), bookshelf structures and recrystallized flakes of quartz.

3.4. Granitic veins

Granitic veins crosscut the syenitic massif (Fig. 3c), granites and orthogneisses. Their thickness varies from centimeter to meter. They are sometimes denuded and outcrop in the shape of centimetric (Fig. 3d) to metric blocks. They are pinkish (Fig. 3d) and their texture is aplitic with the naked eyes. Microscopically, they are granular (Fig. 3e) to suboriented heterogranular (Fig. 3f) and are mainly constituted of quartz (~35%), plagioclase (~35%, orthoclase (~5%), microcline (~20%) and at some places rare green hornblende (~5%), biotite (~2%), opaque oxides (≤ 1%), titanite (≤ 1%) and zircon (~1%). Quartz and feldspar are subrounded to anhedral micro to phenocrysts locally oriented (Fig. 3f). The larger ones are about 1.6 mm. Quartz grains are also amoeboid in shape (Fig. 3e) and flatten at certain places or constitute monomineral clusters. Feldspar crystals have cloudy aspect due to fine flakes of white micas growth (sericitization of plagioclase) or the presence of reddish products. Certain plagioclase crystals show bent polysynthetic twinning and are broken. Some microcline and orthoclase crystals show perthites. Green hornblende, opaque, titanite and zircon crystals are isolated among quartz and feldspars. Opaque crystals are also found as inclusion in green hornblende and plagioclase.

3.5. Orthogneisses

Orthogneissic rocks are found in the western part of granitoids and in the northern part of both syenitic massif and granitoids (Fig. 1c). They are also found encrusted sporadically in granitoids at the southern part

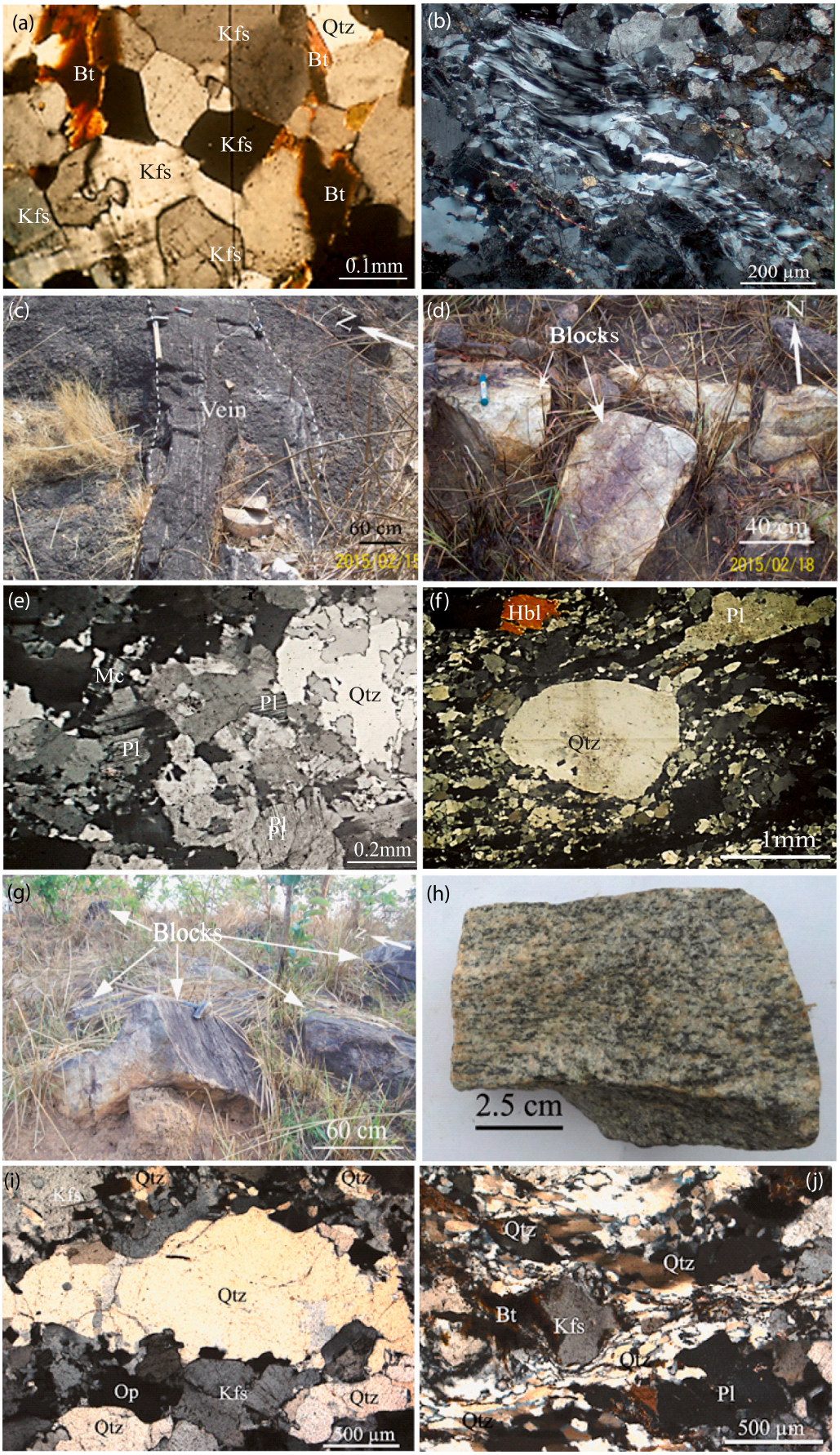

Fig. 3. Selected outcrops, hand samples and microphotographs of granitoids, granitic veins and orthogneisses from the Goa-Mandja area (a, b, e, f, i and j under crossed polarized light). Microphotographs of granites showing (a) a granular texture and (b) fibrous trails of Qtz. (c) Granitic vein cross-cutting syenites and (d) outcropping in the shape of centimetric blocks. Microphotographs of granitic veins showing (e) a granular texture (see the amoeboid Qtz crystal) and (f) sub-oriented heterogranular texture (see the subrounded phenocryt of Qtz surrounded by suboriented microcrysts). (g) Outcrop of orthogneiss in the shape of blocks. (h) Hand sample of orthogneiss showing foliation marked up by a blurred preferred orientation of minerals. Microphotographs of orthogneisses showing heterogranoblastic textures and (i) a subovoid and/or flattened Qtz and (j) Qtz crystals with a stretched sponge feature. Abbreviations: Qtz (quartz), Mc (microcline), Kfs (K-feldspar), Pl (plagioclase), Hbl (hornblende) and Bt (biotite).

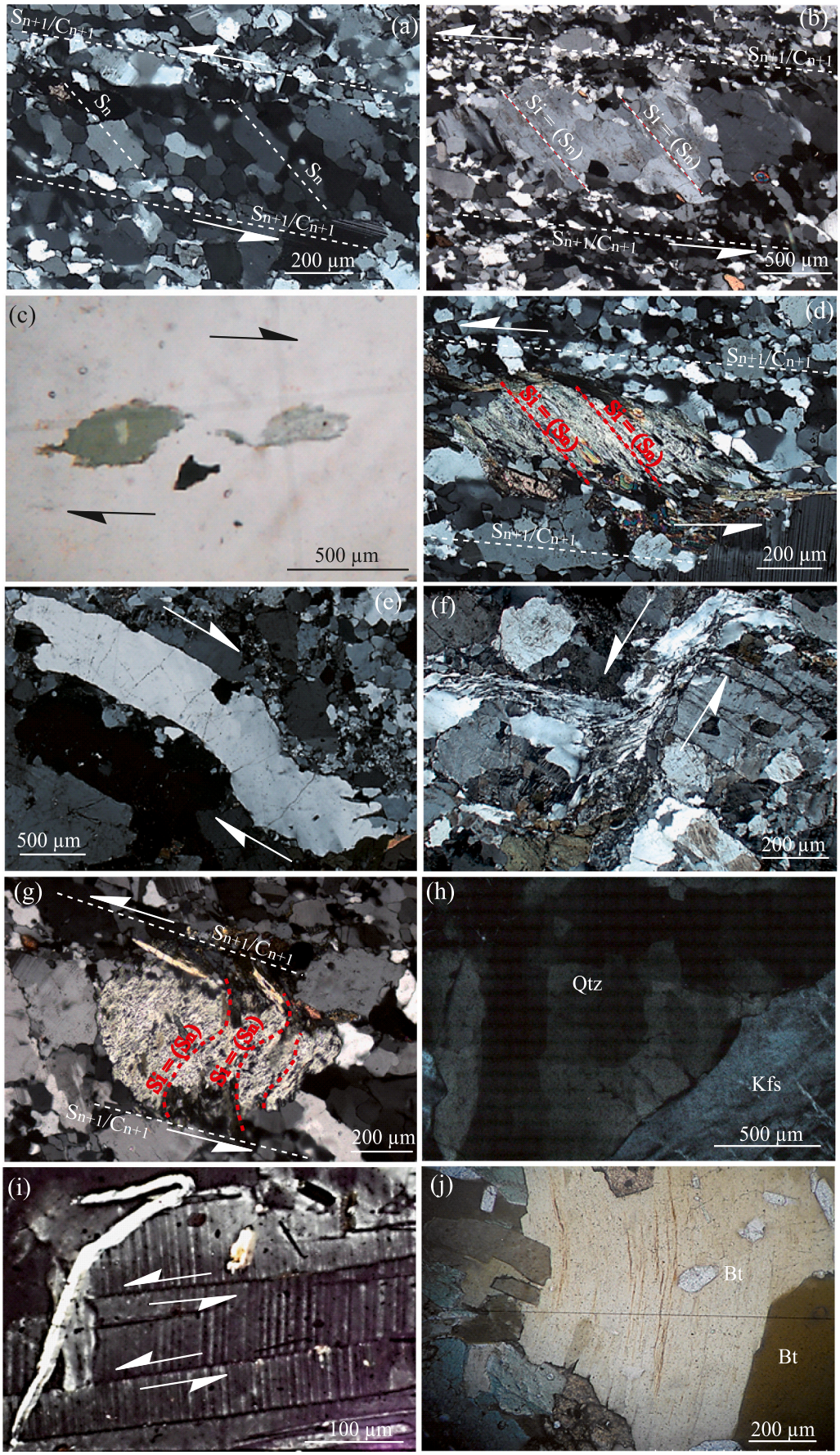

Fig. 4. Selected microphotographs of microstructures and kinematic markers in granitoids from the Goa-Mandja area (a, b, d, e, f, g, h and j under crossed polarized light. c and i under polarized light). (a) S_n foliation marked by the preferred orientation of quartz and feldspar crystals. (b) S_n foliation marked by an internal foliation S_i (=S_n); (a and b) S/C structure combining S_{n+1} and C_{n+1}, and overtaking S_n foliation. (c) Shearband microboudins. (d) Mineral fish showing internal foliation S_i (=S_n) and S/C structure combining S_{n+1} and C_{n+1}, and overtaking S_n. (e) elongated and twisted quartz crystal with stair stepping shape. (f) Recrystallized quartz as fibrous trails following C orientation. (g) S/C structure combining S_{n+1} and C_{n+1}, and overtaking Sn; Z shape rolling structures in green hornblende crystal bearing helicitic inclusions. (h) quartz-chessboard subgrains. (i) Bent cleavages of biotite. (For interpretation of the references to color in this figure legend, the reader is referred to the web version of this article.)

of the syenitic massif. They outcrop in the shape of blocks (Fig. 3g), and boulders with size varying from centimeter to several meters and domes, slabs and chocolate tablet-like of several meters. Their color is grey to pinkish grey and yellowish. They display foliation marked by blurred preferred orientation (N080°E to N090°E and N110°E to N120°E) of minerals (Fig. 3h). Their texture is granoblastic to heterogranoblastic (Figs. 3i, j). The mineralogical assemblage is constituted of anhedral to amoeboid micro to megablasts of quartz (~10–35%), orthoclase (~5–30%), plagioclase (~10–40%), microcline (~10–15%), green hornblende (~2–15%), biotite (~5–15%) and accessory opaque minerals (~1–3%), anhedral, subhedral to euhedral titanite (≤ 1%), apatite (≤ 1%) and zircon (≤ 1%). Quartz blasts are ubiquitous, oriented and or clustered in monomineral assemblages. The larger ones are often subovoid and/or flattened (Fig. 3i). At certain places, quartz seems to present a stretched sponge structure (Fig. 3j) shaping other crystals. Green hornblende blasts are generally associated to biotite, titanite and opaque oxides, with which they constitute discontinuous colored layers disturbed by the presence of quartz and feldspars. Biotite flakes can be skeleton-like and are partially transformed to opaque oxides and chlorite. The presence of apatite and zircon, especially if they are euhedral, is sometimes assumed to indicate magmatic origin (Touret and Huizenga, 2012). Therefore, the estimated modal compositions of orthogneisses have been plotted in the QAP diagram which revealed compositions of granodiorite, quartz monzonites and granites (Fig. 6a).

4. Index of deformation in granitoids at the microscopic scale

Granitoids in the Goa-Mandja area seem to be non-deformed. However, at the microscopic scale, they show signs of deformation. In quartz monzonites, two generations of S foliation are recognizable. The first generation is outlined by a preferred orientation of quartz and feldspar crystals (S_n) (Fig. 4a) and/or an internal foliation S_i (=S_n) (Figs. 4b, d, g). The second generation (S_{n+1}) is underlined by the presence of stretched, flattened and oriented polycrystalline quartz and feldspar ribbons which obliquely overtake the first generation (Figs. 4a, b, d, g). In these rocks, C shear bands (C_{n+1}) parallel to S_{n+1} are recorded. Taken together, they constitute S/C (=S_{n+1} /C_{n+1}) structures (Figs. 4a, b, d, g). One generation of S foliation is also observed in protomylonitic monzonites. It is marked in cataclazed and suboriented granites by planar subarrangement of ferromagnesians. C_{n+1} is also outlined in quartz monzonites by shear band microboudins (Fig. 4c). In protomylonitic monzonites, quartz monzonites, and in granites showing cataclazed portions, C shear bands are marked by the presence of ovoid crystals and mineral fish (Fig. 4d), and twisting of flattened and elongated crystals or polycrystalline quartz, which show stair stepping shape (Fig. 4e). C shear bands are also accompanied by recrystallization where the texture seems to be more cataclazed, producing fibrous trails similar to strain fringes of quartz composition and stretched following C orientation (Fig. 4f). In these rocks, Z shape rolling structures in green hornblende crystals presenting helicitic inclusions are observed (Fig. 4g). In addition to microstructures used in kinematic as S/C, mineral fish, Z shape rolling structures and shear band boudins, other microstructures on the scale of individual or group of crystals have been registered. They are solid state microstructures outlined by internal deformation observed as undulose extinction in quartz, feldspar, and sometimes in biotite crystals. The internal deformation of quartz leads to the formation of quartz-chessboard microstructures (Fig. 4h). Bent twinning, intracrystalline deformation bands (Fig. 4i) of plagioclase crystals and bent cleavages of biotite (Fig. 4j) are found.

Therefore, granitoids have been deformed but with an intensity not allowing deformational structures to be visualized at sample and outcrop scales as foliations in the case of orthogneisses.

5. Analytical methods

A total of seventeen samples (one monzonite, six quartz monzonites, four granites, one granitic vein and five orthogneisses) were selected for whole-rock geochemical analysis (Table 1). Among them, twelve and three samples were, respectively, selected for whole-rock Sr—Nd isotopic and zircon U-Pb-Hf-O isotopic analysis (Table 1).

Altered surfaces of samples are cut off to avoid influence from chemical weathering after emplacement and exposure. Fresh chips of selected samples were cleansed, dried, crushed and pulverized to obtain the appropriate size (200 mesh) of particles, in an agate mill.

The standard crushing, sieving, magnetic and heavy liquid separation methods were used to separate zircon grains. After these operations, individual grains were handpicked under a binocular microscope and mounted together with the reference Penglai and Qinghu zircons in an epoxy resin. The mounted zircon grains were polished to expose 2/3 of the surface of grains, and imaged in reflected and transmitted lights before analysis. Appropriate spots for O and Hf isotopic, U—Pb geochronological analysis were selected based on internal structures revealed through cathode-luminescence (CL) at the State Key Laboratory of Geological Process and Mineral Resources (SKLGPMR), China University of Geosciences (CUG), Wuhan using a Gatan Mono CL4 Cathode-Luminescence detector attached to Zeiss Sigma 300 field emission SEM.

5.1. Oxygen isotopes

The analysis of oxygen isotopes of zircon grains was performed at the SIMS Laboratory of Guangzhou Institute of Geochemistry, Chinese Academy of Sciences (GIGCAS), on a Cameca IMS 1280-HR, through a high-precision secondary ion mass spectrometry (SIMS). The Qinghu (Li et al., 2013) zircon was employed as the unknown sample and yielded values from 5.17‰ ± 0.24‰ to 6.12‰ ± 0.24‰ (2SD) (Supplementary material 1) which are nearly consistent with the indicated value within error (5.39‰ ± 0.22‰ (2SD); Li et al., 2013). The external reference material used in order to calibrate the instrumental mass fractionation was the Penglai zircon (Li et al., 2010). More details of analytical procedure and operating conditions are shown by Yang et al. (2018).

5.2. LA-ICP-MS zircon U—Pb ages and Hf isotope analyses

Zircon U—Pb isotope and trace element contents were performed at the SKLGPMR (CUG, Wuhan), through an Agilent 7500a ICP-MS instrument supplied with a 193 nm ArF excimer laser ablation system with a beam diameter of 32 um, 5 Hz repetition rate for 45 s. The external standard zircon 91,500 was employed and analyzed twice every 5 analysis. For evaluating the data quality of analysis, GJ-1 was determined as unknown sample (Supplementary material 2). Detailed operating conditions for the instrument and data reduction are presented in Liu et al. (2010). ICPMSDataCal (Liu et al., 2010) were used off-line to make raw data reduction analysis. The results of these latter were reported with 1σ error. Concordia diagrams and weighted mean calculations were handled using Isoplot 4.15 (Ludwig, 2012).

In-situ zircon Lu—Hf isotope analyses were conducted at the SKLGPMR (CUG, Wuhan), using a Neptune plus multi-collector (MC)-ICPMS system coupled with a Geolas 193 nm ArF excimer laser ablation system. Avoiding zircon grains showing low concordances and ages which deviate from the majority, measurements were handled on the same grains previously analyzed for U—Pb dating. The laser beam energy density was 5.3 J/cm^2 with a repetition rate of 8 Hz, a spot size of 44 μm in diameter and ablation time of 20 s. In order to evaluate the quality of analysis, zircons Penglai and Plešovice were used as the unknown samples. They give the $^{177}Hf/^{176}Hf$ ratios (Supplementary material 3), respectively consistent within errors with the reported values of 0.282906 ± 0.000010 (Li et al., 2010) and 0.282482 ± 13 (Sláma et al., 2008). Raw data were treated off-line using ICPMSDataCal software (Liu et al., 2010) and the results reported with 2σ error. The following parameters of $^{176}Lu/^{177}Hf_{CHUR}$ = 0.0336 ± 1, $(^{176}Hf/^{177}Hf)_{CHUR}$ = 0.282785 ± 11 (Bouvier et al., 2008);

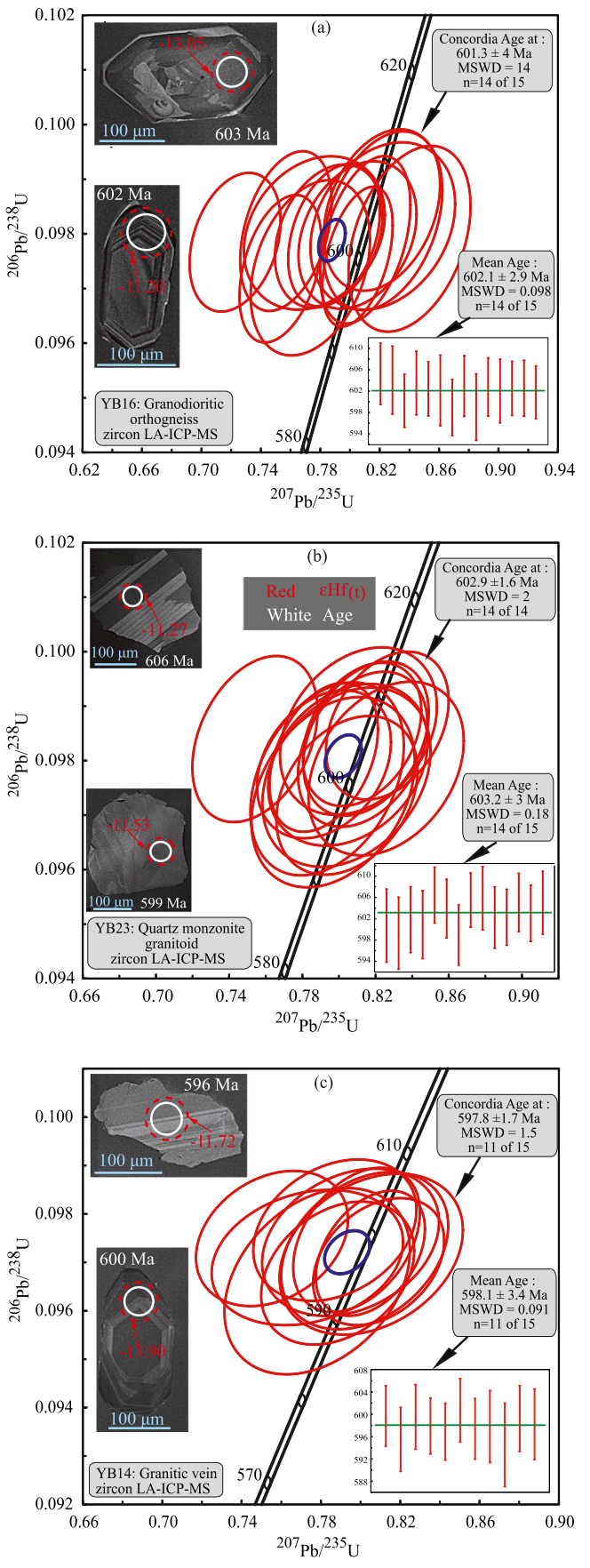

(caption on next column)

Fig. 5. LA-ICP-MS U—Pb zircon age Concordia diagrams, U—Pb zircon weighted mean ages and representative cathode-luminescence (CL) images of dated zircon grains. (a) Orthogneiss sample YB16. (b) Quartz monzonite sample YB23. (c) Granitic vein sample YB14. White circles and numbers indicate the spot locations of U—Pb analyses and corresponding ages. Red dashed circles and numbers show the spot locations of Hf isotope analyses and corresponding εHf (t) values. (For interpretation of the references to color in this figure legend, the reader is referred to the web version of this article.)

$(^{176}Lu/^{177}Hf)_{DM} = 0.0384$, $(^{176}Hf/^{177}Hf)^{DM} = 0.28325$ (Griffin et al., 2000) and $\lambda = 1.867 \times 10^{-11}$ year^{-1} (Söderlund et al., 2004) are used in the calculation.

5.3. Whole-rock major and trace elements geochemistry

Major and trace elements were analyzed at the SKLGPMR (CUG, Wuhan). Major element contents were determined on fused glass disks, using an X-ray fluorescence spectrophotometer (XRF-1800). To verify the analytical precision, international measured standard samples GBW07103, GBW07111, GBW07112, GBW07122 and GBW07123 have been employed as reference materials and have yielded results with an accuracy better than ±5%. The LOI (Loss on Ignition) was determined on 1 g of rock powder after drying at 1000 °C during 90 min.

Trace element contents were determined using ICPMS (inductively coupled plasma mass spectrometry) on an Agilent 7500a ICP-MS. 50 ± 1 mg of sample powder were decomposed by HF + HNO_3 in Teflon bombs. Closed beakers in high-pressure bombs have been used to make sure that the powder has been totally digested. The measured external standard samples AGV-2, BCR-2, BHVO-2, GSP-2 and RGM-2 were used as reference materials and yielded an analytical precision better than 5% for most trace elements.

5.4. Whole-rock Sr—Nd isotopic analyses

The powder (~100 mg) of each selected sample was dissolved in concentrated HF + HNO_3 in Teflon capsules sealed and heated to 190 °C for 48 h. Afterwards, by addition of 1 ml of 6 N HCl and dissolution in 1 ml of 2.5 N HCl, samples are converted into chlorides. The elemental separation and purification of Nd from the final solution was done by conventional cation-exchange technique (Chen et al., 2009). The instrument used to analyze whole-rock Sr—Nd isotopic contents is a Finnigan Triton Ti thermal ionization mass spectrometer (TIMS) situated at SKLGPMR (CUG, Wuhan). The mass fractionation for measured Nd isotopic ratios was corrected through the $^{146}Nd/^{144}Nd$ value of 0.7219. $\varepsilon_{Nd(t)}$ values have been calculated on the basis of the $^{147}Sm/^{144}Nd$ and $^{143}Nd/^{144}Nd$ values of 0.1960 and 0.512630 for the chondritic uniform reservoir (Bouvier et al., 2008). Nd-TDM model age calculations were based on $^{143}Nd/^{144}Nd$ ratio of 0.513151 and $^{147}Sm/^{144}Nd$ ratio of 0.2136 (Liew and Hofmann, 1988) for the present-day depleted mantle.

6. Results

6.1. Geochronology

Data for three representative samples (including one quartz monzonite, one granodiorite (orthogneiss) and the granitic vein) are presented in Supplementary material 2.

6.1.1. Orthogneiss

Zircon grains of the orthogneiss YB16 (Fig. 1c) are mostly euhedral and prismatic with length varying from 150 to 300 µm. They display dark to light luminescence and clear to blurred oscillatory zoning under CL (Fig. 5a). Their shape and oscillatory zoning suggest that they are magmatic zircon grains, consistent with their high Th/U ratios (0.82–1.60). Fourteen of fifteen analyses yielded $^{206}Pb/^{238}U$ apparent ages between 599 and 605 Ma with Concordia and weighted mean ages

Table 2
Whole rock silica contents (wt%), and calculated δ18O (whole rock) (calculated after Valley et al., 1994).

Sample	Rock type	$\delta^{18}O$ (zircon)	SiO_2 (wt%)	$\delta^{18}O$ (WR) (calc.)
YB16	Granodioritic orthogneiss	6.77	64.2	8.20
YB23	Quartz-monzonite	7.17	62.7	8.51
YB14	Granitic vein	6.45	76.2	8.61

of 601 ± 4 and 602 ± 3 Ma, respectively (Fig. 5a). The latter can be interpreted as the crystallization age of the protolith of the orthogneiss sample YB16. The other one apparent age is younger (565 Ma) and has not been integrated in the age calculation because of Pb loss.

6.1.2. Quartz monzonite

Fourteen zircon grains selected from the quartz monzonite YB23 (Fig. 1c) are anhedral, angular and seem to be fragmented. Their length varies between 150 and 250 μm. They are mostly bright and some of them show banded zoning under CL (Fig. 5b). The absence of overgrowths and the high Th/U ratios between 0.92 and 1.46 could be indicator of a magmatic origin. Fourteen analytical spots on zircon grains from sample YB23 define $^{206}Pb/^{238}U$ apparent ages between 599 and 606 Ma with Concordia and weighted mean ages of 603 ± 2 and 603 ± 3 Ma, respectively (Fig. 5b). The latter can be considered as the crystallization age of the concerned sample.

6.1.3. Granitic vein

Zircon grains from granitic vein YB14 (Fig. 1c) are constituted of fragmented anhedral and unfragmented euhedral grains. Anhedral grains display light luminescence and banded zonation, while euhedral grains show slightly light to dark luminescence and clear to cloudy oscillatory zoning under CL (Fig. 5c). Their lengths vary between 150 and 350 μm. The oscillatory zoning, the absence of overgrowths and the high Th/U ratios between 0.96 and 1.51 (zircon grains with concordance degree range 95–99%) suggest a magmatic origin. Eleven of fifteen analysis show concordance degree of 95–99% and yielded $^{206}Pb/^{238}U$ apparent ages between 595 and 601 Ma with Concordia and weighted mean ages of 598 ± 2 and 598 ± 3 Ma, respectively (Fig. 5c). The latter is considered as the crystallization age of the granitic vein YB14 crosscutting the Linte syenitic massif. The other four of the fifteen analysis show low concordance degree (79–88%) and have not been considered in the age calculation.

6.2. Zircon Hf isotope compositions

In situ Hf isotopic compositions of the analyzed zircon grains are shown in Supplementary material 3. The measured $^{176}Hf/^{177}Hf$ ratios of zircon grains vary from 0.281991 to 0.282114, 0.282081 to 0.282114, and 0.282009 to 0.282102 successively in samples YB16, YB23 and YB14. Their corresponding $\varepsilon_{Hf(t)}$ values vary from −15.3 to −11.2, −11.6 to −10.4 and − 14.5 to −11.0 and T_{DM2} ages at 2225–2480 Ma, 2173–2249 Ma and 2209–2426 Ma, respectively (Supplementary material 3).

6.3. Oxygen isotopes

The oxygen isotope data of 45 spots reported in the SMOW scale are shown in Supplementary material 1. Values of the measured $\delta^{18}O_{zircon}$ ($\delta^{18}O_{zrn}$) for the sample YB23 range between 6.80 and 7.47‰, with a mean of 7.17 ± 0.19‰ (2SE, n = 15). The calculated whole rock $\delta^{18}O$ ($\delta^{18}O_{WR}$) value (Table 2) following empirical correlation $\delta^{18}O_{zrn}$ versus SiO_2 (whole-rock) (Valley et al., 1994) averages 8.51‰ for SiO_2 content of 62.68%. Zircon grains from the sample YB16 yield the measured $\delta^{18}O_{zrn}$ values between 6.09 and 7.67‰, with a mean of 6.77 ± 0.22‰ (2SE, n = 15). The calculated average $\delta^{18}O_{WR}$ value is 8.20‰ for SiO_2 content of 64.17%. The $\delta^{18}O$ values of zircon grains from granitic vein (YB14) ranged from 3.79 to 7.13‰. The average is of 6.45 ± 0.21‰ (2SE, n = 15). The calculated magmatic $\delta^{18}O_{WR}$ is 8.61‰ for SiO_2 content of 76.16%.

6.4. Whole-rock geochemistry

The analytical data of seventeen samples of granitoids, orthogneisses and vein from the Goa-Mandja area are listed in Table 3.

6.4.1. Major elements

The studied rocks are generally silica rich (SiO_2 of 59.7–71.9 wt% in granitoids, 64.2–77.2 wt% in orthogneisses and 76.2 wt% in the granitic vein). The CaO, MgO and Fe_2O_3 contents are higher in monzonitic granitoids than in other rocks. Considered together, all samples have variable abundances of Al_2O_3, K_2O and total alkalis (K_2O + Na_2O: monzonitic rocks = 7.79 to 8.74 wt%, granites = 8.62 to 9.23 wt%, granitic vein = 8.59 wt% and orthogneisses = 6.94 to 10.64 wt%; Table 3). The K_2O/Na_2O ratio is 0.69 for the granitic vein, between 0.95 and 1.55 for monzonitic granitoids, from 0.99 to 1.66 in granites, and from 0.81 to 3.65 in orthogneisses (Table 3). The Al saturation index A/CNK (= molar $Al_2O_3/(CaO + Na_2O + K_2O)$) (Table 3) ranged from 0.83 to 0.98 for monzonitic granitoids, 0.99 to 1.03 for granites, 0.91 to 1.05 for orthogneisses and is 1.02 for the granitic vein (Fig. 6c). The Harker variation diagrams show sub-clustered distribution of sample points with decreasing sub-linear variation trends for MgO and CaO (Figs. 7c, d). This observation can be extended to TiO_2, Al_2O_3, P_2O_5, Fe_2O_3 and MnO, which show slightly scattered plots, but with general negative trends with increasing SiO_2 contents (Figs. 7a, b, g, h, i). Rocks with A/CNK between 0.82 and 0.91 show SiO_2 < 65 wt% (59.70–64.17 wt%), and high TiO_2 (0.70–0.89 wt%), CaO (3.25–4.27 wt%), Fe_2O_3 (4.64–5.80 wt%), MgO (1.54–2.70 wt%), P_2O_5 (0.17–0.37 wt%), and MnO (0.05–0.09 wt%) contents. Rocks with SiO_2 > 65 wt% are metaluminous to peraluminous (0.95 ≤ A/CNK ≤ 1.05). That can suggest different magmatic origins or different evolutions from the same origin. In the diagram of Frost et al. (2001), the studied rocks are dominantly alkali-calcic to alkali (Fig. 6d), except for orthogneisses YB16, YB18 and YB3, which are calc-alkalic. The overall samples display high-K calc-alkaline to shoshonitic affinity (Peccerillo and Taylor, 1976; Nardi et al., 2021; Fig. 6e).

6.4.2. Trace elements

The total rare earth elements (ΣREE) concentrations are variable (121.9–870.9 ppm) with an exceptional low value for the granitic vein (18.07 ppm) (Table 3). The Chondrite-normalized rare earth element patterns (Fig. 8) are characterized by light rare earth elements (LREE) enrichment, heavy rare earth elements (HREE) depletion and the presence or not of Eu anomaly (Eu/Eu* = 0.15–1.15, with an exceptional low value of 0.08 for the orthogneiss sample YB17). On the whole, these patterns are similar (Fig. 8i), suggesting that if different sources exist, they could have similar geochemical characteristics, except the granitic vein, which shows a different profile and relatively lower concentrations of REEs than other rocks (Fig. 8i). The primitive mantle-normalized spiderdiagrams (Fig. 8) are characterized by large ion lithophile elements (LILE) enrichment and remarkable negative Nb, Ta and Ti anomalies and positive K and Pb (except orthogneiss YB17) anomalies. The presence of negative Ti and Eu anomalies in certain samples could be the result of fractional crystallization of ilmenite and plagioclase, respectively. The Nb/Ta ratio is 9.40 for the granitic vein, 12.03–25.50 (average of 17.44) for monzonite, 9.95–19.75 (average of 15.34) for granites and 9.43–24.91 (average of 15.60) for orthogneisses. The averages of Nb/Ta ratios are above the average level of the crust (12.2, Rudnick and Fountain, 1995), apart from the granitic vein which is below. This latter displays a relatively lower pattern in primitive mantle-

Table 3
Major (wt%) and trace (ppm) element data of granitoids and orthogneisses from the Goa-Mandja area.

	monzonite	Q monzonite						granitic vein	granite				orthogneiss				
	Y1	Y4	Y6	Y6'	YB23	YBS2	YBq9	YB14	Y2	YB3	YB5	Y5	YB16	YB17	YB18	YB3'	Y12
Major elements (wt%)																	
SiO_2	59.70	67.33	63.00	62.80	62.68	68.05	63.38	76.16	69.43	69.59	71.88	68.80	64.17	66.58	77.23	74.95	67.37
TiO_2	0.78	0.41	0.74	0.75	0.71	0.42	0.74	0.03	0.36	0.37	0.26	0.32	0.89	0.20	0.10	0.32	0.36
Al_2O_3	16.52	15.48	14.86	14.90	15.61	15.16	14.38	13.05	14.91	15.18	13.90	15.52	14.97	15.67	11.43	12.12	16.69
Fe_2O_3	5.49	3.09	5.51	5.52	4.64	2.70	5.59	0.51	2.31	1.99	2.05	2.27	5.80	4.21	1.80	2.68	1.81
MnO	0.09	0.05	0.09	0.09	0.08	0.05	0.09	0.01	0.04	0.06	0.03	0.04	0.08	0.11	0.01	0.04	0.02
MgO	2.77	1.43	2.03	2.06	2.10	0.98	2.01	0.10	0.82	0.66	0.35	0.91	1.55	0.07	0.07	0.30	0.80
CaO	4.27	2.38	3.26	3.26	3.40	2.05	3.31	0.37	1.83	1.39	0.99	1.87	3.77	1.31	0.33	1.07	2.55
Na_2O	3.56	4.26	3.43	3.48	3.96	4.26	3.46	5.07	4.32	4.00	3.43	4.05	3.84	4.55	1.83	3.23	4.53
K_2O	4.23	4.07	5.32	5.26	4.47	4.49	5.26	3.52	4.30	5.23	5.70	4.63	3.10	6.08	6.67	4.68	4.32
P_2O_5	0.38	0.19	0.21	0.21	0.28	0.17	0.21	0.01	0.15	0.16	0.08	0.11	0.18	0.02	0.02	0.06	0.10
LOI	0.22	0.54	0.45	0.28	0.33	0.25	0.20	0.32	0.61	0.42	0.55	0.79	0.69	0.39	0.13	0.07	0.83
TOL	98.01	99.23	98.90	98.59	98.26	98.57	98.63	99.14	99.08	99.04	99.21	99.31	99.03	99.21	99.63	99.52	99.39
FeOt	4.94	2.78	4.95	4.97	4.18	2.43	5.03	0.46	2.08	1.79	1.85	2.04	5.22	3.79	1.62	2.41	1.63
K2O + Na2O	7.79	8.33	8.74	8.74	8.43	8.74	8.72	8.59	8.62	9.23	9.13	8.68	6.94	10.64	8.51	7.92	8.85
K2O/Na2O	1.19	0.95	1.55	1.51	1.13	1.05	1.52	0.69	0.99	1.31	1.66	1.14	0.81	1.34	3.65	1.45	0.95
A/CNK	0.91	0.98	0.86	0.86	0.89	0.97	0.83	1.02	0.99	1.03	1.02	1.03	0.91	0.95	1.05	0.98	0.99
AI	47.18	45.26	52.36	52.08	47.16	46.38	51.79	39.92	45.40	52.24	57.83	48.29	37.88	51.21	75.72	53.64	41.93
Mg#	0.36	0.34	0.29	0.29	0.33	0.29	0.29	0.18	0.28	0.27	0.16	0.31	0.23	0.02	0.04	0.11	0.33
Trace elements (ppm)																	
Li	16.36	26.29	13.53		21.69	24.68	3.36	0.88	8.53	17.37	14.59	20.17	13.77	10.67	0.77	8.16	11.00
Be	3.01	3.52	3.54		2.31	3.35	8.74	6.12	3.10	3.28	2.96	3.71	2.01	2.89	0.35	2.09	1.97
Sc	14.61	6.74	14.67		11.26	4.83	2.06	0.88	4.22	2.95	2.08	5.37	13.16	4.14	1.39	2.72	1.92
V	116.62	55.79	95.17		88.03	42.66	26.12	3.17	33.63	14.01	17.10	34.48	77.84	1.52	11.03	9.11	39.78
Cr	43.71	33.21	55.12		48.26	14.64	1.29	0.40	11.69	6.85	0.69	20.46	10.46	0.29	0.35	0.60	5.37
Co	125.78	8.41	14.18		108.28	6.13	1.88	0.23	4.74	2.93	1.84	153.45	88.29	0.36	1.01	2.09	5.91
Ni	30.50	17.64	29.85		33.63	9.19	2.89	0.45	7.53	4.18	1.14	23.42	11.88	0.48	1.45	0.72	4.27
Cu	35.21	5.31	12.50		18.29	11.23	11.88	1.26	3.52	7.15	2.13	3.14	9.38	0.76	5.02	4.08	9.80
Zn	75.18	65.71	88.48		82.03	65.04	18.19	11.30	61.48	64.07	38.44	48.29	63.73	67.52	9.52	51.95	29.77
Ga	20.80	22.22	21.79		21.71	23.46	19.49	21.41	22.36	20.55	19.77	21.15	20.08	27.56	12.40	17.68	17.80
Rb	109.43	120.51	132.75		98.32	142.79	163.87	210.06	127.46	185.11	177.82	132.80	73.60	172.84	100.18	167.57	105.71
Sr	849.11	1048.41	1115.07		1216.30	849.04	493.56	105.45	822.25	327.50	298.91	782.34	394.51	54.11	297.19	256.47	967.30
Y	34.23	11.75	24.78		19.35	9.85	15.05	4.12	10.05	59.23	21.14	20.91	28.87	52.54	28.87	84.54	7.96
Zr	299.25	166.99	293.34		257.61	185.42	141.76	39.76	185.13	190.47	253.22	146.29	335.39	611.15	617.46	392.04	255.59
Nb	14.12	8.87	16.13		12.53	8.48	19.63	8.34	8.38	18.92	15.78	9.18	16.89	75.49	0.56	19.36	5.67
Mo	0.69	0.36	0.43		0.31	0.24	8.59	0.07	0.18	0.42	0.52	0.40	0.64	3.48	0.10	0.35	0.53
Sn	2.59	1.24	2.20		1.99	1.50	1.81	1.07	1.37	2.63	1.93	1.29	1.83	2.42	0.41	3.21	0.53

	monzonite	Q monzonite						granitic vein	granite				orthogneiss				
	Y1	Y4	Y6	Y6'	YB23	YBS2	YBq9	YB14	Y2	YB3	YB5	Y5	YB16	YB17	YB18	YB3'	Y12
Trace elements (ppm)																	
Cs	1.23	1.65	0.45		0.40	0.85	1.54	2.96	0.57	1.44	1.08	0.66	0.21	0.33	0.32	0.95	0.76
Ba	1549.98	2050.12	3050.01		2809.77	2188.89	955.61	111.69	1850.26	1399.85	816.18	1750.59	828.07	134.21	1288.04	1114.51	2008.72
La	82.32	27.47	49.10		61.67	46.47	25.88	4.56	35.54	32.28	63.45	44.01	25.62	219.15	80.35	38.78	41.77
Ce	146.18	51.28	94.95		116.34	86.78	64.84	8.45	66.75	101.67	123.81	65.36	47.66	410.69	100.49	86.49	78.40
Pr	15.79	6.05	10.79		12.64	8.69	7.23	0.76	7.26	8.67	13.34	8.42	5.55	41.33	18.14	10.11	8.09
Nd	59.16	23.61	42.86		47.84	32.46	26.34	2.17	27.26	35.22	48.54	33.35	23.29	141.04	69.15	43.64	27.79
Sm	10.73	4.37	8.14		8.39	5.09	4.65	0.31	4.69	8.21	8.74	6.19	5.51	19.65	11.58	11.06	4.02

(*continued on next page*)

Table 3 (*continued*)

	monzonite	Q monzonite						granitic vein	granite				orthogneiss				
	Y1	Y4	Y6	Y6'	YB23	YBS2	YBq9	YB14	Y2	YB3	YB5	Y5	YB16	YB17	YB18	YB3'	Y12
Eu	2.05	1.23	2.22		2.17	1.41	0.94	0.08	1.23	1.73	0.89	1.57	1.75	1.53	2.33	1.48	1.09
Gd	7.66	3.01	6.06		5.57	3.28	3.11	0.30	3.03	7.49	5.81	5.07	4.93	13.12	8.05	11.34	2.42
Tb	1.03	0.37	0.80		0.70	0.38	0.45	0.05	0.36	1.30	0.75	0.65	0.80	1.73	0.98	1.97	0.28
Dy	5.85	2.02	4.38		3.67	1.86	2.62	0.39	1.72	9.08	3.68	3.59	4.83	9.52	5.18	12.83	1.38
Ho	1.16	0.37	0.87		0.65	0.33	0.48	0.09	0.33	1.93	0.66	0.70	1.01	1.91	0.96	2.82	0.27
Er	3.09	0.99	2.21		1.67	0.82	1.30	0.33	0.85	5.84	1.77	1.84	2.64	4.99	2.49	7.60	0.69
Tm	0.44	0.14	0.32		0.24	0.12	0.20	0.06	0.11	0.91	0.31	0.28	0.41	0.76	0.37	1.27	0.10
Yb	2.66	0.89	1.97		1.50	0.74	1.27	0.45	0.77	5.99	2.24	1.73	2.54	4.74	2.32	7.48	0.63
Lu	0.40	0.15	0.29		0.22	0.11	0.17	0.07	0.12	0.82	0.34	0.27	0.38	0.69	0.38	1.09	0.10
Hf	7.43	4.08	6.88		6.07	4.83	3.42	1.52	4.67	4.76	7.08	3.76	7.99	14.30	16.09	10.56	6.02
Ta	1.06	0.55	0.71		0.84	0.33	1.63	0.89	0.42	1.39	0.88	0.92	1.43	3.03	0.06	1.34	0.33
Pb	24.12	30.81	25.88		27.78	33.20	47.51	49.50	35.39	30.32	39.88	33.68	10.94	7.41	35.38	31.08	26.51
Bi	0.02	0.05	0.01		0.01	0.01	0.03	0.03	0.02	0.02	0.02	0.00	0.01	0.01	0.01	0.03	0.01
Th	21.54	9.71	7.27		5.62	8.34	25.86	25.75	34.57	11.59	42.21	12.60	2.56	23.79	18.82	10.47	8.96
U	0.97	2.85	0.56		0.43	1.07	2.97	3.64	4.52	2.38	4.81	1.29	1.65	2.62	1.23	2.43	0.55
ΣREE	338.52	121.94	224.96		263.27	188.54	139.48	18.07	150.01	221.13	274.31	173.04	126.92	870.86	302.76	237.95	167.03
Eu/Eu*	0.48	1.08	0.94		0.94	1.12	0.56	0.60	0.99	0.46	0.15	0.73	1.05	0.08	0.54	0.16	1.15
Rb/Sr	0.13	0.11	0.12		0.08	0.17	0.33	1.99	0.16	0.57	0.59	0.17	0.19	3.19	0.34	0.65	0.11
Ba/Rb	14.16	17.01	22.98		28.58	15.33	5.83	0.53	14.52	7.56	4.59	13.18	11.25	0.78	12.86	6.65	19.00
Nb/Ta	13.38	16.04	22.73		14.96	25.50	12.03	9.40	19.75	13.65	18.00	9.95	11.85	24.91	9.43	14.47	17.36
Ce/Pb	6.06	1.66	3.67		4.19	2.61	1.36	0.17	1.89	3.35	3.10	1.94	4.35	55.42	2.84	2.78	2.96
Nb/U	14.56	3.11	28.87		29.02	7.92	6.61	2.29	1.86	7.94	3.28	7.09	10.21	28.78	0.46	7.95	10.24
TZr (°C)	782.66	772.60	792.03		782.31	788.17	710.46	671.10	795.40	809.95	852.38	773.07	811.30	946.95	1003.21	906.78	822.55

Note:FeOt = Fe2O3*0.8998; Mg# = [MgO/(MgO + FeOt)]; LOI: loss on ignition; A/CNK molar = Al2O3/(CaO + Na2O + K2O); A/NK molar = Al2O3/(Na2O + K2O).
AI = 100(K2O + MgO)/(K2O + MgO + Na2O + CaO) (Ishikawa et al., 1976); Subscript N = chondrite-normalized value from Sun and McDonough (1989).
TZr: zircon saturation temperature (after Boehnke et al. (2013)).

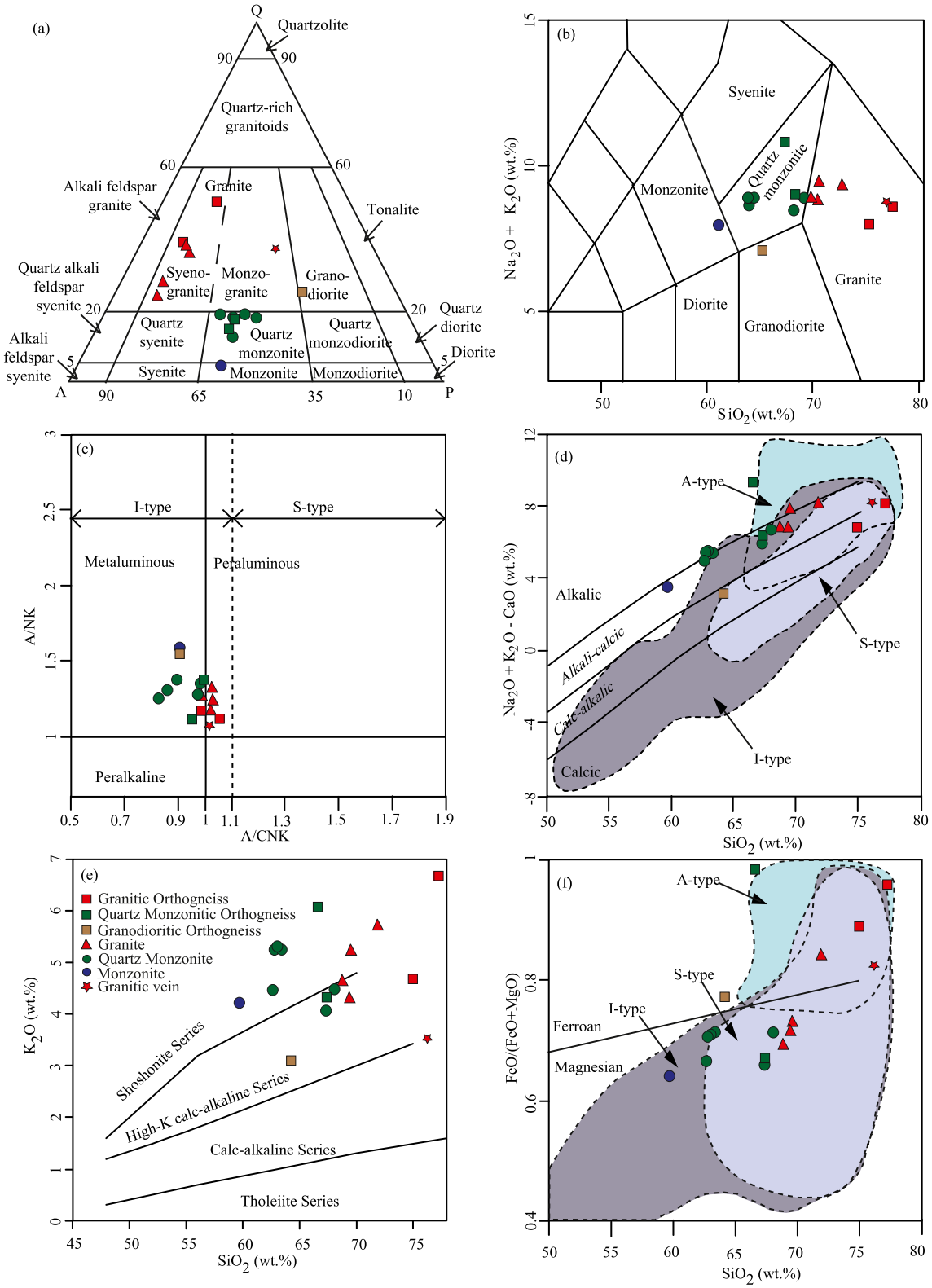

Fig. 6. (a) Petrographical classification (QAP diagram) and (b) Silica (wt%) vs. total alkali ($Na_2O + K_2O$) (wt%) (Middlemost, 1994) of granitoids, orthogneisses and granitic vein from the Goa-Mandja area. Geochemical classification of the studied rocks. (c) Shand's index molar $Al_2O_3/(CaO + Na_2O + K_2O)$ vs. $Al_2O_3/(Na_2O + K_2O)$ diagram (after Maniar and Piccoli, 1989). (d) silica (wt%) vs. $(Na_2O + K_2O)$-CaO (wt%) (Frost et al., 2001). (e) Silica (wt%) vs. K_2O (wt%) (Peccerillo and Taylor, 1976). (f) Silica (wt%) vs. FeO/(FeO + MgO) (Frost et al., 2001).

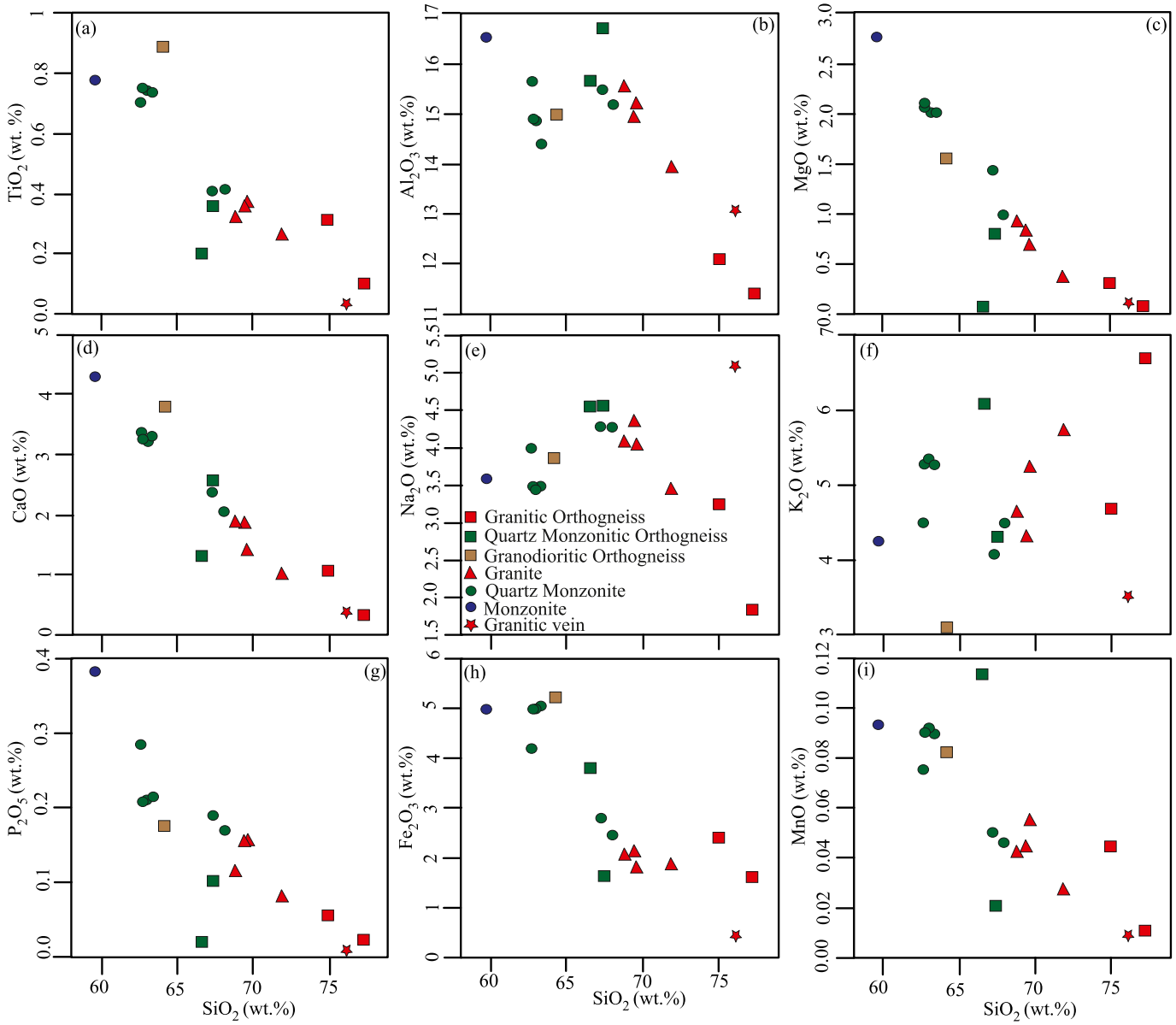

Fig. 7. Selected silica (wt%) vs. major elements (wt%) diagrams for granitoids, orthogneisses and granitic vein from the Goa-Mandja area.

normalized spiderdiagram compared to those of the other rocks (except for elements such as Cs, Rb, Th, Nb and Ta) (Fig. 8j).

6.5. Whole-rock Sr—Nd isotopic compositions

A total of twelve samples were analyzed for whole-rock Sr and Nd isotopes (Table 4). Initial $^{87}Sr/^{86}Sr$ ratios and $\varepsilon_{Nd(t)}$ were calculated back to the crystallization ages of 602 Ma (orthogneiss), 603 Ma (quartz monzonite) and 598 Ma (granitic vein) obtained in this study. The crystallization age of quartz monzonites (603 Ma) is used to calculate the initial $^{87}Sr/^{86}Sr$ ratios and $\varepsilon_{Nd(t)}$ of granites because they could be cogenetic based on the similarities of their REE and trace element patterns as well as their mixed nature in the outcrop. The granites, monzonitic rocks, orthogneisses and granitic vein have initial $^{87}Sr/^{86}Sr$ ratio of 0.706496 to 0.708121, 0.704841 to 0.707662, 0.705107 to 0.758215 and 0.703328, respectively. Their $\varepsilon_{Nd(t)}$ values range from −1.7 to −1.8, −9.9 to 0.0, −21.9 to +1.6 and + 5.7, respectively. The model ages (T_{DM2}) are 1455–1466 Ma for granites, 1321–2120 Ma for monzonitic rocks, 1188–3084 Ma for orthogneisses and 854 Ma for the granitic vein (Table 4).

7. Discussion

7.1. Widespread magmatism at ~600 Ma within the CAFB

The U—Pb zircon ages representing granitoids (603 ± 3 Ma), orthogneisses (602 ± 3 Ma) and granitic veins (598 ± 3 Ma) indicate that the crystallization times of these rocks are similar within error and could be globally related to the same geological activities affecting different sources or protoliths during the Pan-African orogeny. These ages are similar within error to the 603 ± 4 and 600 ± 3 Ma ages obtained in the Linte massif (Yomeun et al., 2022), 602 ± 1.4 Ma in the Batié porphyrogranite (Njiekak et al., 2008), 600 ± 3.7 Ma in the Bapa-Batié biotite-amphibole granite (Chebeu et al., 2011) in the west Cameroon and 601 ± 1 Ma (zircon evaporation age) in the Meiganga amphibole-biotite granite (Ganwa et al., 2011) in the west and east of the Adamawa-Yade. The 603 ± 3 Ma, 602 ± 3 Ma and 598 ± 3 Ma ages in the Goa-Mandja area are also similar to the 591 ± 19 Ma age recorded in the Rocher du Loup metasyenites (e.g., Lerouge et al., 2006) in the northwestern corner of the Congo Craton and to 602 ± 5 Ma recorded in the Correntes pluton (Silva Filho et al., 2016), in the Pernambuco-

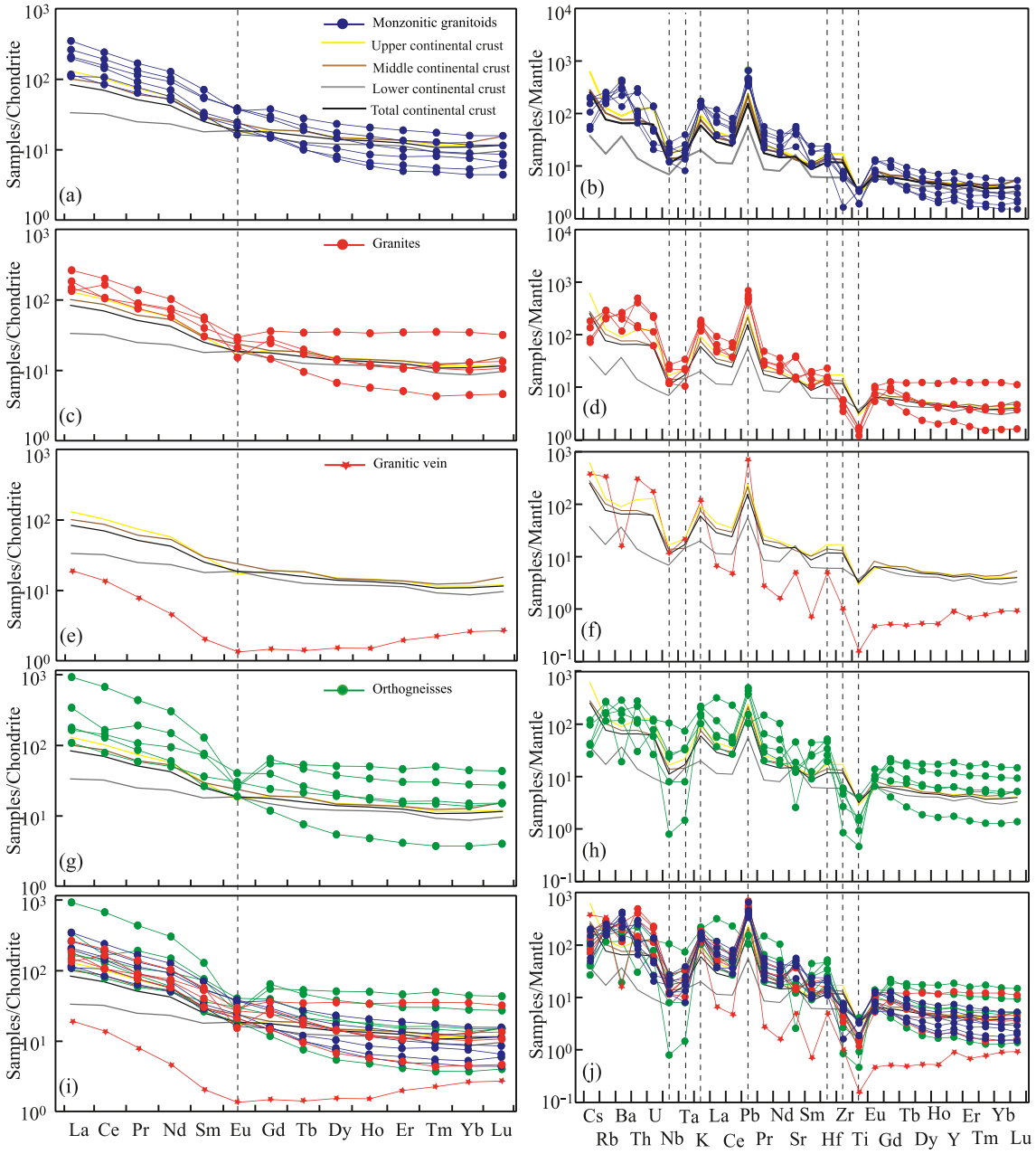

Fig. 8. Chondrite-normalized REE and Primitive Mantle-normalized trace element patterns for (a, b) monzonites, (c, d) granites, (e, f) granitic vein and (g, h) orthogneisses from the Goa-Mandja area. (i) Combination of (a), (c), (e) and (g). (j) Combination of (b), (d), (f) and (h). The upper, middle, lower and total continental crust values are from Rudnick and Gao (2003), and the Chondrite and the Primitive Mantle normalizing values are from Sun and McDonough (1989).

Alagoas (PEAL) crustal domain of the Brasiliano orogeny (branch of the Pan-African orogeny in northeastern Brazil). All these synchronous ages indicate widespread magmatism at about 600 Ma within the CAFB in Cameroon and within its extension in northeastern Brazil.

Beside the ~600 Ma old magmatism in the Goa-Mandja and other areas shown above, a large interval of Neoproterozoic ages (between ca. 690 and ca. 545 Ma) have been reported in the Adamawa-Yade domain and parts of the Cameroon territory to the west of the TBF (Table 5). Comparatively to recent works from southern Chad, the magmatism tends to be older in Cameroon (≥ 600 Ma) and becomes younger in Chad (595–590 Ma) (Shellnutt et al., 2017, 2020, 2021).

7.2. *Effect of alteration*

The studied rocks show gneissic and submylonitic foliations at certain places, the presence of fine dust of secondary muscovite and red weathered products in certain plagioclases, partial transformation of green hornblende to biotite and primary biotite to chlorite, suggesting varied degrees of metamorphism and alteration. However, the alteration index (Ishikawa et al., 1976) AI <60 (37.88–57.83) (Table 3) suggests that these rocks are unaltered apart from the orthogneiss sample YB18 with AI = 75.72. In addition, transition elements, LILE, REE and HFSE are not totally destabilized (excepted in quartz monzonite YBq9 and orthogneisses YB17, YB18 and YB3') in regard to sub-linear correlations of some selected elements from these latter groups (e.g., TiO_2, Fe_2O_3, K_2O, Rb, Hf, Y, Nb, Sm and Nd) versus more alteration-resistant element such as Zr (Wang et al., 2018) (Fig. 10). This suggests that these elements could have more or less conserved their primitive characteristics in most of the studied samples. Therefore, some transition elements, LILE, REE and HFSE elements will be considered to discuss petrogenesis

Table 4
Sr and Nd data for samples from the Goa-Mandja granitoids and orthogneisses.

Sample	Rock type	U-Pb age	Rb (ppm)	Sr (ppm)	$^{87}Sr/^{86}Sr$	$^{87}Rb/^{86}Sr$*	$^{87}Sr/^{86}Sr$	Sm (ppm)	Nd (ppm)	$^{147}Sm/^{144}Nd$	$^{143}Nd/^{144}Nd$	εNd (t)	TDM1	TDM2
		Ma			measured		initial				measured		(Ma)	(Ma)
Y1	monzonite	603	109	849	0.708048	0.3729	0.704841	10.7	59.2	0.109586	0.512288	−0.01	1263	1321
Y4	quartz monzonite	603	121	1048	0.709359	0.3326	0.706499	4.37	23.6	0.111876	0.511792	−9.88	2029	2120
YB3	granite	603	185	327	0.722186	1.6355	0.708121	8.21	35.2	0.140783	0.51232	−1.79	1735	1466
YB5	granite	603	178	299	0.721299	1.7214	0.706496	8.74	48.5	0.108836	0.512201	−1.65	1380	1455
YB23	quartz monzonite	603	98.3	1216	0.709673	0.2339	0.707662	8.39	47.8	0.105970	0.511788	−9.50	1924	2090
YB16	granodioritic orthogneiss	602	73.6	395	0.727305	0.5399	0.72267	5.51	23.3	0.142833	0.511301	−21.9	3946	3084
YB17	quartz monzonitic orthogneiss	602	173	54.1	0.838572	9.3601	0.758215	19.6	141	0.084179	0.511771	−8.16	1622	1981
YB18	granitic orthogneiss	602	100	297	0.715073	0.9754	0.706699	11.6	69.2	0.101172	0.512339	1.62	1100	1188
YB3`	granitic orthogneiss	602	168	256	0.724271	1.8905	0.708041	11.1	43.6	0.153094	0.512422	−0.76	1831	1381
Y12	quartz monzonitic orthogneiss	602	106	967	0.707822	0.3162	0.705107	4.02	27.8	0.087424	0.512206	0.08	1141	1313
YBq9	quartz monzonite	603	164	494	0.714927	0.9607	0.706665	4.65	26.3	0.106757	0.511857	−8.21	1841	1986
YB14	granitic vein	598	210	105	0.752484	5.7642	0.703328	0.31	2.17	0.087256	0.512495	5.69	792	854

* $^{87}Rb/^{86}Sr$ were calculated from Rb and Sr elemental ICPMS data.

and geodynamic implication of the studied rocks.

7.3. Petrogenesis of the Goa-Mandja rocks

7.3.1. Classification of rocks

The classification diagram of Middlemost (1994) displays a succession of monzonite, quartz monzonites and granites for granitoids; granodiorite, quartz monzonites and granites for orthogneisses and granite for the vein rock (Fig. 6b), which is consistent with the nomenclature revealed by the petrographic analysis through the QAP diagram (Fig. 6a). The compositions of these rocks are varied and the molar A/CNK of monzonitic granitoids ranging from 0.83 to 0.98 indicate metaluminous character (Fig. 6c). Granites, granitic vein and orthogneisses samples with A/CNK values ranging between 0.91 and 1.05 are metaluminous to weakly peraluminous (Fig. 6c). The A/CNK of all these rocks (< 1.1) conforms to I-type (Fig. 6c) granitoids (Chappell and White, 1992). The modified alkali-lime index (MALI) ($Na_2O + K_2O$-CaO) and the FeOt/(FeOt+MgO) versus SiO_2 discrimination diagrams (Frost et al., 2001) revealed that the studied rocks are dominantly alkali-calcic with some of them encroaching the calc-alkalic and alkalic fields (Fig. 6d) and display magnesian to ferroan character (Fig. 6f). They have high-K calc-alkaline to shoshonitic affinity (Fig. 6e) and mostly occur within the fields of I-type granites in the MALI and the FeOt/(FeOt+MgO) versus SiO_2 diagrams (Figs. 6d, f). They show negative correlation between P_2O_5 and SiO_2 (Fig. 7g), a common feature of I-type granites. In addition to the presence of hornblende, the studied rocks could be classified as I-type granitoids as those described in west Cameroon (e.g., Djouka-Fonkwé et al., 2008; Kwékam et al., 2010, 2020a, 2020b; Ngo Belnoun et al., 2013).

7.3.2. Processes modifying magma compositions

The studied rocks (except granitic vein YB14) show similar patterns in Chondrite-normalized and primitive mantle-normalized spider diagrams, but variation exists in specific elements (Fig. 8), which could be attributed to assimilation and fractional crystallization (FC). The horizontal to subhorizontal trends in $(^{87}Sr/^{86}Sr)_i$ vs. SiO_2 and vs. 1/Sr *1000 (Figs. 11a, b) indicate significant fractional crystallization of crustal rocks after magma generation. The correlation between the $\varepsilon_{Nd(t)}$ vs. SiO_2 (Fig. 11c) shows a more complex evolution with crustal contamination and assimilation coupled with fractional crystallization (AFC). However, it is still dominated by the process of fractional crystallization outlined by the sub-horizontal trend. Moreover, zircon grains from these rocks have relatively constant and consistent Hf isotopic compositions (Fig. 12a), indicating assimilation is not the process controlling the magma evolution in the present case. Negative Eu, Nb, Ta and Ti anomalies (Fig. 8) indicate the crystallization of minerals, such as plagioclase, hornblende, biotite and titanite. However, the positive Eu anomalies with Eu/Eu* values of 1.08, 1.12, 1.05 and 1.15, respectively, in monzonites Y4 and YBS2 and in orthogneisses YB16 and Y12, reveal that these latter rocks contain a small quantity of cumulate plagioclase. Negative correlations between TiO_2, Al_2O_3, MgO, CaO, P_2O_5, Fe_2O_3, MnO, and SiO_2 (Fig. 7) suggest also that fractional crystallization could have intervened during magmatic evolution. Inverse correlations of SiO_2 with MgO, P_2O_5 and Fe_2O_3 (Figs.7c, g, h) suggest separation of apatite and mafic minerals during crystallization. Anticorrelations between TiO_2, Fe_2O_3 and SiO_2 (Figs. 7a, h) as well as a negative Ti anomaly (Figs. 8b, d, f, h, j) indicate the fractionation of magnetite and titanite. Variation of Ba and Sr contents in the studied rocks could be the result of fractional crystallization. The depletion of Ba content (from 3050 to 111.7 ppm) in the Ba versus Rb diagram (Fig. 11d) and the decrease of Sr (from 1216 to 54.1 ppm) in the Ba versus Sr (Fig. 11e) are consistent with K-feldspar fractionation. The trend marked by rocks in the Rb/Sr versus Sr diagram (Fig. 11f) can be interpreted as evidence of K-feldspar and plagioclase fractionation. Plagioclase fractionation could be also supported by the negative correlation between Al_2O_3, CaO and SiO_2 (Figs. 7b, d). Besides, the zonation shown by certain plagioclase and K-feldspar crystals can also support that FC has played an important role in the magma evolution.

7.3.3. Constraints on magma source region

The negative sub-linear trends of major oxides such as TiO_2, MgO, CaO, P_2O_5, Fe_2O_3 and MnO vs. SiO_2 (Fig. 7) and relative similarities in the Chondrite-normalized REE patterns suggest that the source(s) of these rocks could be geochemically cogenetic (apart from the granitic vein) (Fig. 8). Samples show similarities with crustal rocks in regard to LILE (e.g., Rb, K) and LREE enrichments (Fig. 8) and HFSE (e.g., Nb, Ta, Ti) depletions (Fig. 8). Nevertheless, these trace element patterns show more LILEs enrichment than the lower continental crust (Fig. 8). The

Table 5
Geochronological data for the emplacement age (between ca. 690 and ca. 545 Ma) of Neoproterozoic plutonic rocks in the Adamawa-Yade domain and parts of the Cameroon territory to the west of the TBF.

Locality	Rock type	Age	Method	Reference
southeast of Lomié	Metagabbro	666 ± 26 Ma	U-Pb zircon dating	Toteu et al. (2006b)
west of Poli	Metadiorite	665 ± 10 Ma	U-Pb zircon dating	Toteu et al. (2006a)
Linte	Syenite	662 ± 4 Ma	U-Pb zircon dating	Yomeun et al. (2022)
Linte	Monzonite	633 ± 3 Ma	U-Pb zircon dating	Yomeun et al. (2022)
Bep	Granitic orthogneiss	641 ± 2 Ma	U-Pb zircon dating	Tchakounté et al. (2017)
Bapé	Monzodioritic orthogneiss	628 ± 3 Ma	U-Pb zircon dating	Tchakounté et al. (2017)
Bangwa	Metaleucogranite	638 ± 2 Ma	U-Pb zircon dating	Njiekak et al. (2008)
Bangwa	Metagranodiorite	637 ± 5 Ma	U-Pb zircon dating	Njiekak et al. (2008)
Tonga	Synkinematic granitoid	618 ± 20 Ma	U-Pb zircon dating	Njiosseu et al. (2005)
Batié	Amphibole and biotite granites	ca. 630 to 547 Ma	U-Pb zircon dating	Kwékam et al. (2020b)
Bapa-Batié	Biotite granite	619 ± 19 Ma	U-Pb zircon dating	Chebeu et al. (2011)
Meiganga	Dioritic protholith	637 ± 5 Ma	U-Pb zircon dating	Ganwa et al. (2018)
Ngaoundéré	Biotite-muscovite granitoid	615 ± 27 Ma	Th-U-Pb monazite dating	Tchameni et al. (2006)
Ngaoundéré	Biotite granitoid	ca. 575 Ma	Th-U-Pb monazite dating	Tchameni et al. (2006)
Fomopea	Diorite	621 ± 3 Ma	U-Pb zircon dating	Kwékam et al. (2010)
Fomopea	Quartz-monzodiorite	613 ± 2 Ma	U-Pb zircon dating	Kwékam et al. (2010)
Bangangte	Monzonite	585 ± 4 Ma	U-Pb zircon dating	Tchouankoue et al. (2016)
Bangangte	Syenite	583 ± 4 Ma	U-Pb zircon dating	Tchouankoue et al. (2016)
Dschang	Biotite granite	578 +7/−11 Ma	U-Pb zircon dating	Kwékam et al. (2020a)
Dschang	Magnetite granite	563 +8/−3 Ma	U-Pb zircon dating	Kwékam et al. (2020a)
Bafoussam	Two-mica granitoids	558 ± 8 Ma to 564 ± 7 Ma	Th-U-Pb monazite dating	Djouka-Fonkwé et al. (2008)
Wum	Two-mica granite	561 ± 3 Ma	U-Pb zircon dating	Li et al. (2017)
Wum	Undeformed biotite granite	557 ± 4 Ma	U-Pb zircon dating	Li et al. (2017)

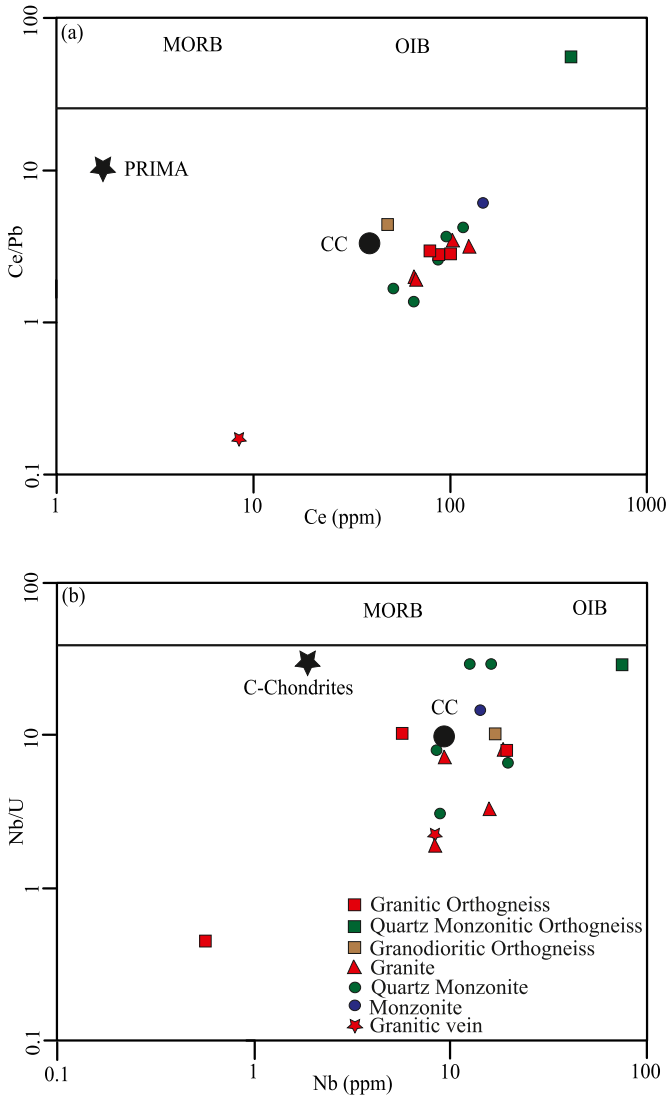

Fig. 9. Plots of (a) Ce/Pb vs. Ce (ppm) and (b) Nb/U vs. Nb (after Hofmann et al., 1986) showing most of studied rocks in the field of continental crust. CC (continental crust).

distribution of most of the studied samples in the Ce/Pb versus Ce (Fig. 9a) and Nb/U versus Nb (Fig. 9b) diagrams of Hofmann et al. (1986) points to continental crust composition. However, some samples near or within the mantle-OIB domain could suggest a slight presence of mantle components in the sources. A similar case has been reported in the I-type granites from Dschang in the northern domain (Kwékam et al., 2020a). The slightly elevated $\delta^{18}O_{zrn}$ (except the lowest 3.79‰ in the granitic vein) and $\delta^{18}O_{WR}$ values of rocks are indicative of crustal rocks as the magma source, which experienced low-temperature water-rock interaction (e.g. Wang et al., 2017). The crustal origin can be also supported by the relatively moderate to high contents of SiO_2 (59.70–77.23 wt%), and low contents of MgO (0.07–2.77 wt%), Cr (0.29–55.12 ppm), Ni (0.45–33.63 ppm) and V (1.52–116.62 ppm). Furthermore, the $Mg^{\#}$ ($Mg^{\#}$ = [MgO/(MgO + FeOt)]) values <0.40 (0.02–0.36) corroborate that the studied rocks could result from the amphibolitic/basaltic lower continental crust melts irrespective of the degree of melting (e.g., Rapp and Watson, 1995). The high positive $\varepsilon_{Nd(t)}$ (+5.69) of the granitic vein could indicate derivation from relatively juvenile source. However, the low $Mg^{\#}$ (0.18), low MgO (0.10 wt%) and the high SiO_2 (76.16 wt%) of this latter rock rule out the possibility of its derivation directly from the mantle. Therefore, the juvenile Neoproterozoic crust could be considered as the probable source for the granitic vein as the case of granites to the west of the Chad Lineament ($\varepsilon_{Nd(t)}$ values = +1.3 to +7.0, Isseini et al., 2012; Shellnutt et al., 2018). These data suggest that the studied rocks could result from partial melting of continental crust. The K_2O contents of 3.10 to 6.67 wt% and the positive K anomalies (Figs. 8b, d, f, h, j) suggest medium- to high-K phase, which could be related to the presence of K-feldspar and biotite in the sources of these rocks. This could be the result of a slight upper crust contamination (slightly shown in the $\varepsilon_{Nd(t)}$ vs. SiO_2 plot; Fig. 11c) and fractional crystallization as the lower crust is generally depleted of high-K phases like K-feldspar and biotite.

Zircon Hf data are relatively constant between −15.3 and − 10.4 and consistent among samples, which could mean relatively homogeneous sources. However, in general, a slight Nd—Hf decoupling is observed

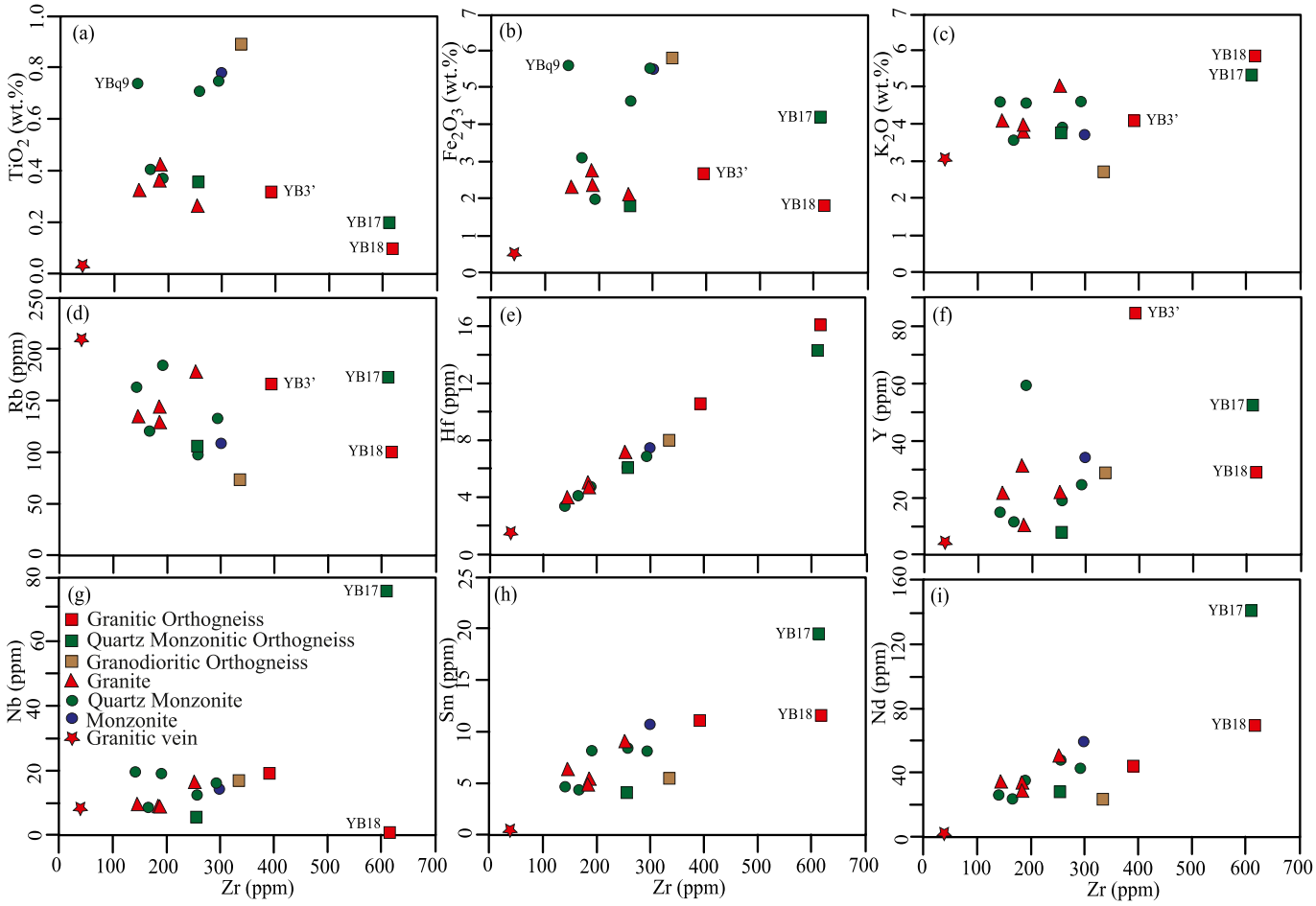

Fig. 10. Selected major (wt%) and trace elements (ppm) vs. Zr (ppm) for the granitoids, orthogneisses and granitic vein from the Goa-Mandja area.

(Figs. 12a, b) in some samples. The $\varepsilon_{Nd(t)}$ versus MgO plot shows a negative correlation, while the $\varepsilon_{Hf(t)}$ versus MgO plot shows a slight sub-horizontal trend or no obvious correlation (Figs. 12c, d), suggesting anomalous behavior of Hf isotopes. Therefore, the low to medium variable initial $^{87}Sr/^{86}Sr$ ratios of 0.703328–0.722670 (except orthogneissYB17 which has value of 0.758215) and variable positive to negative (+5.7 to −9.9 except very low −21.9 in orthogneiss YB16) $\varepsilon_{Nd(t)}$ values (Fig. 12e), combined with the diversity of Nd-T_{DM2} could support the heterogeneity of crustal protoliths and sources for the granitic vein, granitoids and orthogneisses, and probably the multi-pulse of magmas during a short interval of time (~5 Ma) as indicated by the crystallization ages between 598 and 603 Ma. The lowest $\varepsilon_{Nd(t)}$ of −21.9 in orthogneiss YB16 could be related to the local mixing of crustal protolith with an Archean heritage (Nd-T_{DM2} at 3084 Ma). Such remark (εNd(600 Ma) of −18.73 and Archean Nd-T_{DM} at 2524 Ma; Ngamy Kamwa et al., 2019) has been shown in one sample of quartz monzonite from the Yoro-Yangben area located at about 100 km to the southwest of the Goa-Mandja area. The high initial $^{87}Sr/^{86}Sr$ ratio revealed in orthogneiss YB17 (0.758215) could result from alteration. This latter sample shows high Rb/Sr (3.19) and low Ba/Rb (0.78) ratios, low Ba (134.21 ppm) and Sr (54.11 ppm) contents compared to the other studied orthogneisses (Rb/Sr of 0.11–0.65; Ba/Rb of 6.65–19.00; Ba of 828–2010 ppm and Sr from 256 to 967 ppm), granitoids and granitic vein (Rb/Sr of 0.08–1.99; Ba/Rb of 0.53–28.6; Ba of 112–3050 ppm and Sr of 105–1216 ppm), and the bulk continental crust (Rb/Sr = 0.15; Ba/Rb = 9.31; Ba = 446 ppm; Sr = 320 ppm; Rudnick and Gao, 2003). Feldspar and biotite alterations could be associated with Sr and Ba depletions. The Rb/Sr and Ba/Rb ratios are, respectively, higher and lower in rocks showing pronounced alterations (e.g., Ekwere, 1985; Imeokparia, 1981).

The heterogeneous continental protoliths should contain an Archaean portion as the orthogneiss sample YB16 shows Nd-T_{DM2} age of 3084 Ma. Mesoproterozoic to Paleoproterozoic and Neoproterozoic crusts should have also contributed, since most of Nd-T_{DM2} ages range between 1188 and 2120 Ma, with one younger age at 854 Ma obtained in the granitic vein. A similar case, but without Neoproterozoic T_{DM} age has been described in the west of Cameroon (e.g., Kwékam et al., 2010). However, the zircon Hf-T_{DM2} reveals only Paleoproterozoic ages (2173–2480 Ma), which are characteristic of the North and West Cameroon to the west of the TBF. Therefore, the location of the studied rocks in the Adamawa-Yade domain could be the symbol of the transition between the Adamawa-Yade and the northern domains. The 854–3084 Ma interval of Nd-T_{DM2} ages in this study is also close to the distribution of Sm—Nd T_{DM} ages in the Pernambuco-Alagoas domain (~900–3000 Ma) (e.g., Silva Filho et al., 2016; Van Schmus et al., 2008), known as the extension of the northern domain of CAFB in northeastern Brazil.

7.3.4. *Temperature-oxygen fugacity conditions*

The solubility of zircon is related to zirconium concentration, temperature and major element composition of the melt. Zircon saturation temperatures (T_{Zr}) of magma are estimated using zirconium concentrations of melt through the equation $T_{Zr}(K) = (10108)/[1.16\ (M\text{-}1) + 1.48 + \ln(500{,}000/Zr_{melt})]$ (Boehnke et al., 2013). Based on the Zr content of the studied rocks, the T_{Zr} ranged from 710 to 788 °C with an average of 771 °C in monzonitic rocks, 773 to 852 °C with an average of 808 °C in granites, 811 to 1003 °C with a mean of 898 °C in orthogneisses and 671 °C in the granitic vein (Table 3). The mean values of T_{Zr}

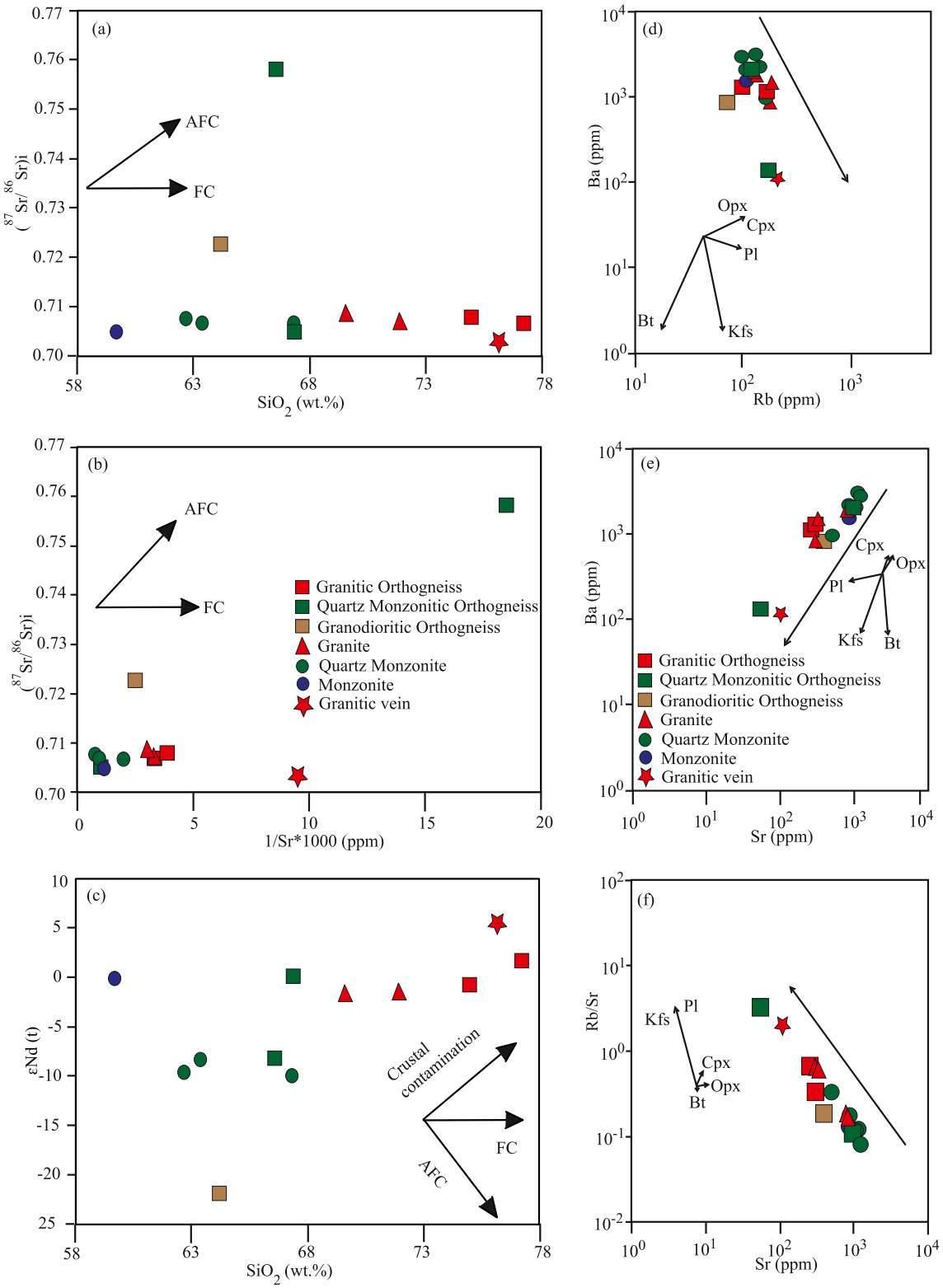

Fig. 11. Plots of (a) silica (wt%) vs. initial ($^{87}Sr/^{86}Sr$), (b) silica (wt%) vs. 1/Sr*1000 (ppm) and (c) silica (wt%) vs. $\varepsilon_{Nd(t)}$ indicating dominant fractional crystallization. (d) Rb (ppm) vs. Ba (ppm) and (e) Sr (ppm) vs. Ba (ppm) showing K-feldspar fractionation. (f) Sr (ppm) vs. Rb/Sr (ppm) showing K-feldspar and plagioclase fractionation.

in granites and orthogneisses are consistent with fairly hot granitoids (T_{Zr} > 800 °C; Miller et al., 2003). They are also higher than the temperature obtained in the typical I-type granites (781 °C, e.g., Chappell and White, 1992). The mean value in monzonitic rocks and the value in the granitic vein point to a much colder granitoid (T_{Zr} < 800 °C; Miller et al., 2003). However, the mean value of T_{Zr} in monzonitic rocks is relatively similar to the I-type granites (781 °C, e.g., Chappell and White, 1992), while the value in the granitic vein is low. Therefore, the studied rocks could be considered as normal to high temperature I-type granitoids (except the granitic vein; T_{Zr} = 671 °C).

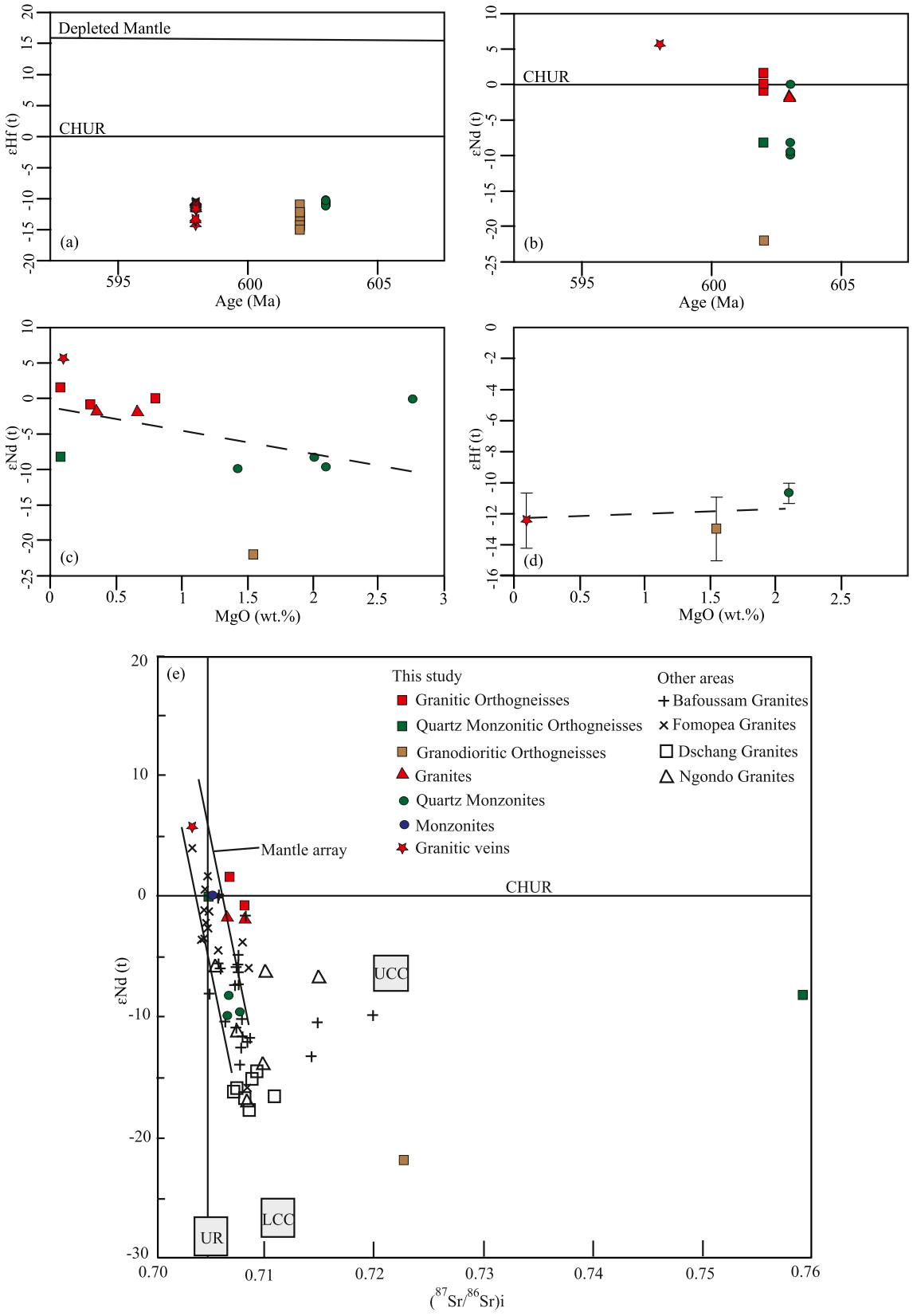

Fig. 12. Plots of (a) U—Pb zircon age vs. $\varepsilon_{Hf(t)}$, (b) U—Pb zircon age vs. $\varepsilon_{Nd(t)}$, (c) MgO (wt%) vs. $\varepsilon_{Nd(t)}$ and (d) MgO (wt%) vs. $\varepsilon_{Hf(t)}$ for granitoids, orthogneisses and granitic vein from the Goa-Mandja area. (e) Plot of initial ($^{87}Sr/^{86}Sr$) vs. $\varepsilon_{Nd(t)}$ from this study and published data of granites from Bafoussam (Djouka-Fonkwé et al., 2008), Ngondo (Tagne-Kamga, 2003), Fomopea and Dschang (Kwékam et al., 2020b) in western Cameroon. The LCC (Lower continental crust) and UCC (Upper continental crust) fields. CHUR (Chondritic uniform reservoir), UR (Uniform reservoir).

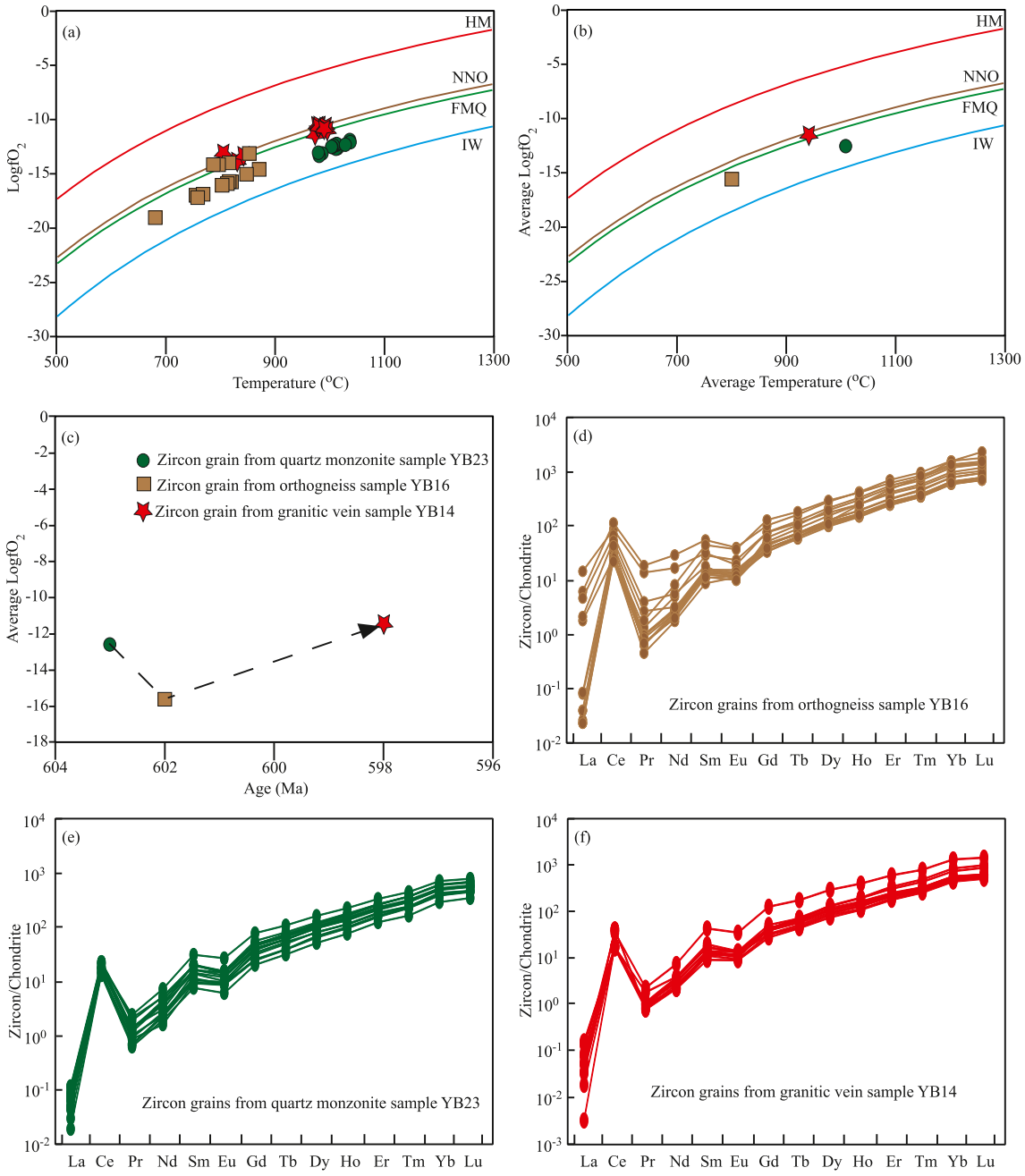

Fig. 13. (a) Ti-in-zircon temperature (°C) vs. logfO_2, (b) Average Ti-in-zircon temperature (°C) vs. Average logfO_2. (c) U—Pb age vs. Average logfO_2. Zircon REE chondrite-normalized patterns for orthogneiss (d), quartz monzonite (e) and granitic vein (f). NNO (Ni-NiO), FMQ (fayalite-magnetite-quartz), IW (iron-wustite) and HM (hematite-magnetite).

Important information of the crystallization conditions can be obtained through Ti-in-zircon temperatures. These latter have been estimated following the equation: T (°C) = 4800/(5.711-log(Ti-in-zircon)-log(a_{SiO2}) + log(a_{TiO2}))-273 of Ferry and Watson (2007). Activities of SiO_2 (a_{SiO2}) and TiO_2 (a_{TiO2}) are respectively set to 1 and 0.6, since quartz is present in the studied rocks while rutile has not been found. The calculated Ti-in-zircon temperatures (Supplementary material 4) for selected samples YB16 (orthogneiss), YB23 (quartz monzonite) and YB14 (granitic vein) (except zircon grains showing low concordances), respectively, range from 681 to 870 °C (average of 799 °C), 979 to 1038 °C (average of 1009 °C) and 806 to 996 °C (average of 942 °C). These values of Ti-in-zircon temperatures are consistent with the intervals 574–1137 °C recently shown in the neighboring rocks of the Linte area (Ayonta Kenne et al., 2021) and 678–1013 °C in the Linte syenitic massif (Yomeun et al., 2022) and could suggest high degree melting, presumably at the lower crust (Ayonta Kenne et al., 2021, and references therein).

The fO_2 (calculated through the template proposed by Loucks et al. (2020) without respect to pressure values) shown in Supplementary material 4, range, respectively, from −19.03 to −13.05, −13.38 to −11.87 and − 13.79 to −10.48 with the respective averages of −15.59, −12.56 and − 11.44 in the samples YB16, YB23 and YB14. The position of these data in Ti-in-zircon temperatures vs. logfO_2 (Fig. 13a, b) shows that the points of zircon grains from YB16 and YB23 samples are collectively below the FMQ (fayalite-magnetite-quartz) buffer, indicating crystallization under reduced conditions for granitoids and orthogneisses, while the points of zircon grains from sample YB14 are slightly above the FMQ buffer, implying slightly oxidized magmatic

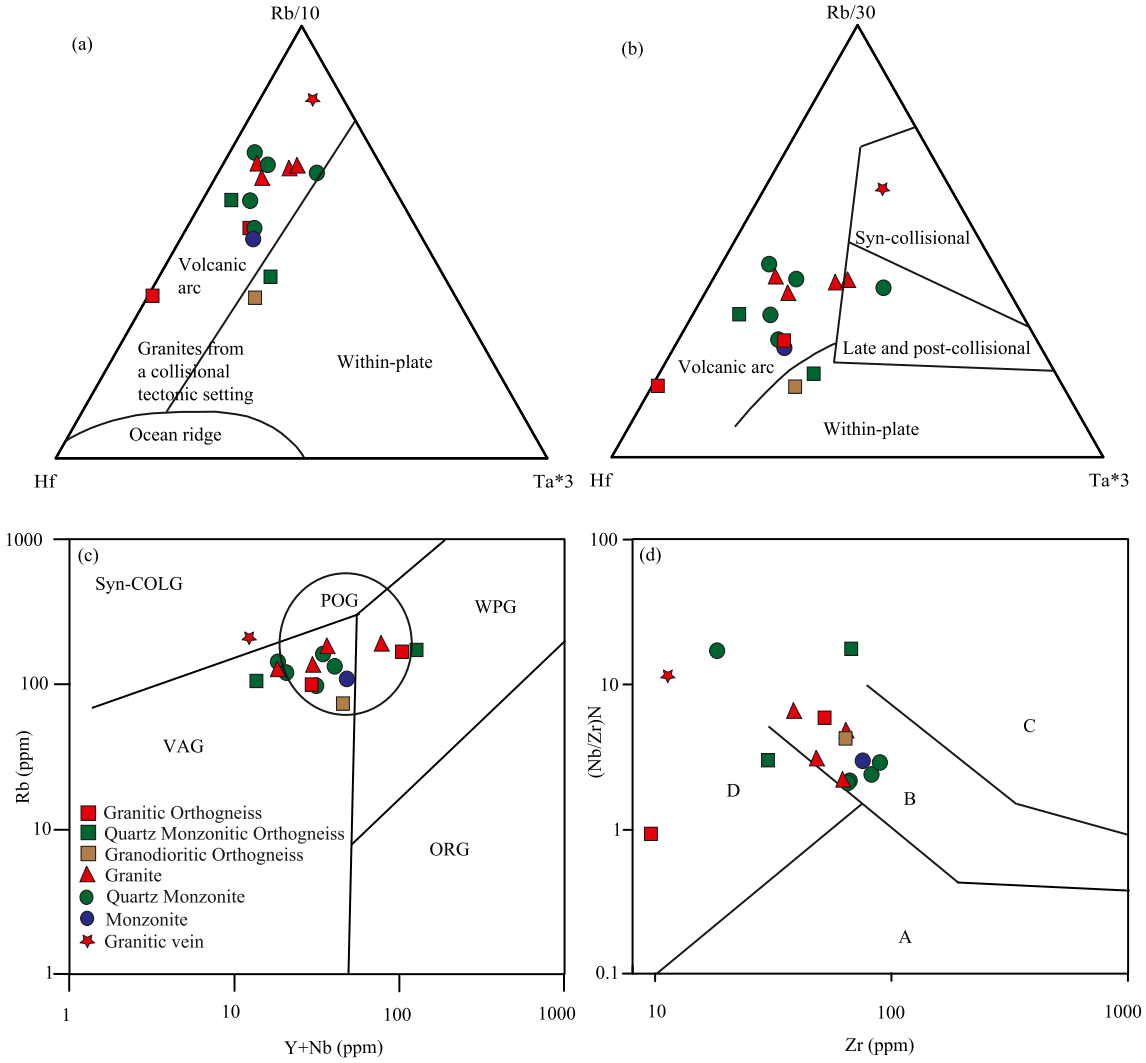

Fig. 14. Plots for geochemical tectonic discriminant diagrams for granitoids, orthogneisses and granitic vein from the Goa-Mandja area. (a) Rb/10-Hf-Ta*3 and (b) Rb/30-Hf-Ta*3 discrimination triangle diagrams (after Harris et al., 1986). (c) Rb (ppm) vs. (Y + Nb) (ppm) (after Pearce et al., 1984 and Pearce, 1996). (d) Zr (ppm) vs. $(Nb/Zr)_N$ (after Thiéblemont and Tegyey, 1994). VAG (Volcanic arc granite), WPG (Within plate granite), Syn-COLG (Syn-collision granite), ORG (Ocean ridge granite), POG (post-collision granite), A (subduction zone), B (continent-continent collision zone), C (alkaline intraplate zone), D (peraluminous continent-continent collision zone).

conditions for granitic veins. The average logfO_2 versus ages diagram shows fO_2 variation in sources with a decreasing order from 603 to 602 Ma, and a relatively increasing order at 598 Ma (Fig. 13c). The selected zircon grains are depleted and enriched in LREE and HREE successively, as shown in the Chondrite normalized REE patterns (Fig. 13d, e, f). They also exhibit strong positive Ce (Ce/Ce* with $Ce^* = Nd_N^2/Sm_N$) anomalies (Fig. 13d, e, f) from 7.35 to 85.17 in YB16, 12.38 to 49.69 in YB23 and 21.99 to 112.40 in YB14 (Supplementary material 4), and negative Eu ($Eu/Eu^* = Eu_N/(Sm_N{*}Gd_N)^{1/2}$) anomalies (Fig. 13d, e, f) from 0.09 to 0.43 (average of 0.27), 0.20 to 0.33 (average of 0.25) and 0.19 to 0.41 (average of 0.26), respectively, in the same latter samples (Supplementary material 4). Rocks from oxidized magmas show zircon Eu/Eu* values generally higher than 0.4 (Zhu et al., 2018). In zircon grains of the granitic vein, these anomalies could be the result of plagioclase fractionation and magma with a moderate oxidized composition, in which there are strong incorporations of Ce^{4+} (Trail et al., 2012) even if their zircon Eu/Eu* values are in general lower than 0.4. In the orthogneiss and granitoid zircon grains, these Eu/Eu* values (with averages much lower than 0.4) could also indicate plagioclase fractionation and reduced conditions in their sources.

7.4. Tectonic setting and geodynamic implications

7.4.1. Tectonic setting of rocks

The studied rocks are generated from crustal sources with probable requirement of substantial transient heat flux. Common heat sources can be related to underplating of sub-continental lithosphere mantle-derived mafic magmas and upwelling asthenosphere, which induced partial melting of the lower crust (e.g., Pe-Piper et al., 2009; Toledo and de Assis Janasi, 2021).

The studied rocks show significant arc related signatures such as LILE and LREE enrichment and HFSE depletion (Fig. 8). They are mostly plotted within the volcanic arc field with a weak extension of few samples in the within plate rocks field, *syn*-collision rocks field and late and post-collision rocks field in the Rb/10-Hf-Ta*3 and Rb/30-Hf-Ta*3 discrimination diagrams of Harris et al. (1986) (Fig. 14a, b) and in the Rb vs. Y + Nb tectonic discrimination diagram of Pearce et al. (1984) (Fig. 14c). They mostly occur within or near the field of post-collisional granitoids (POG) of Pearce (1996) (except granitic vein YB14 and orthogneiss Y12) (Fig. 14c). In the Zr vs. (Nb/Zr)N diagram (Thiéblemont and Tegyey, 1994, Fig. 14d), most of the studied rocks are within the collision zone.

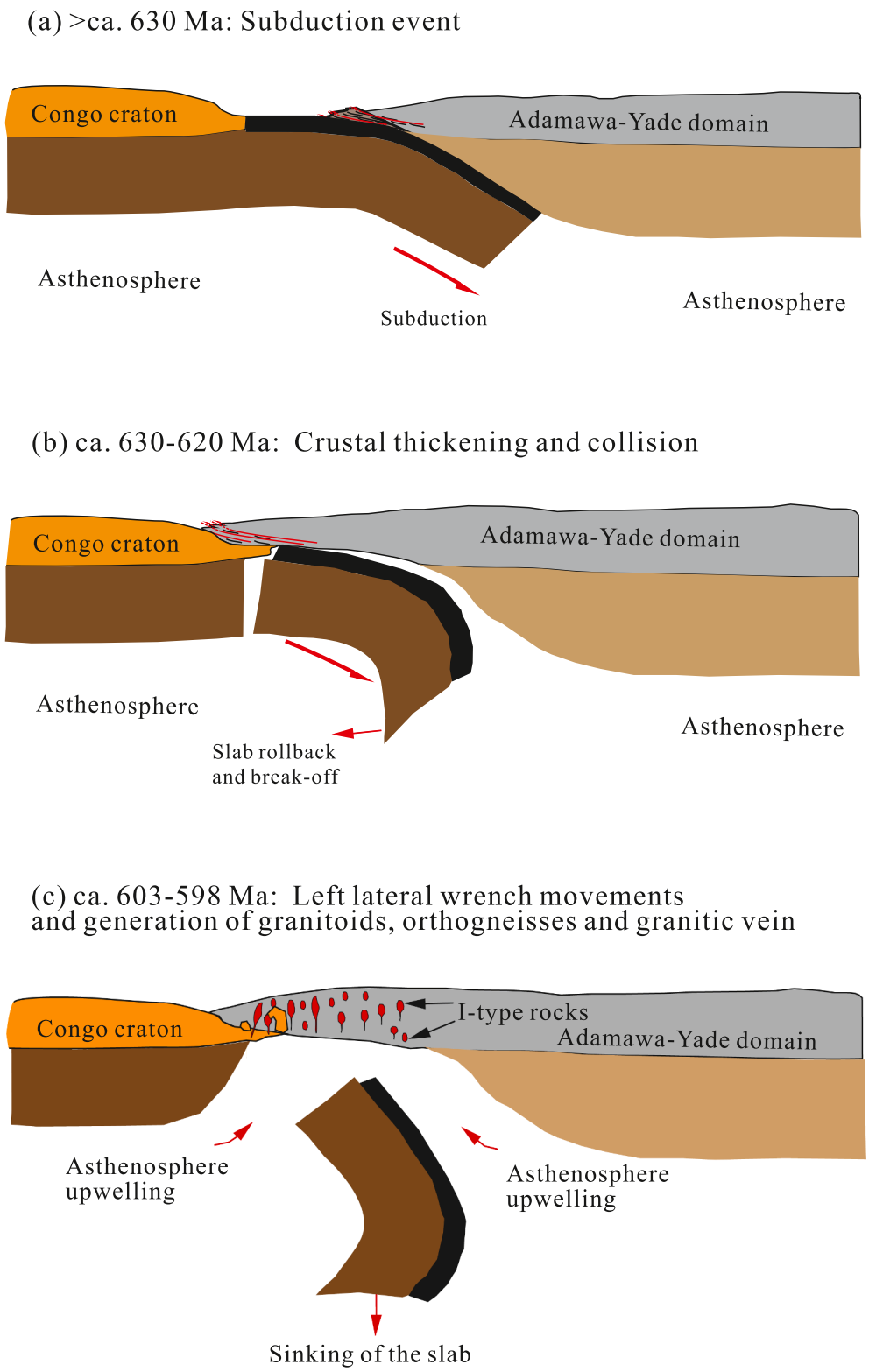

Fig. 15. Schematic representation of the geodynamic evolution of the Goa-Mandja area during (a) subduction event (> ca. 630 Ma), (b) Crustal thickening and collision (ca. 630–620 Ma) and (c) Left lateral wrench movements and generation of granitoids, orthogneisses and granitic vein (ca. 603–598 Ma).

The potassic alkali-calcic to shoshonitic feature (Fig. 6e), the arc related feature (Figs. 14a. b, c) and the high-temperature I-type granitoids feature suggest that the studied rocks could originate from magmas related to a subduction zone as is the case of the Batie granites (Kwékam et al., 2020b). Rocks display LILE enrichment and significant negative Nb, Ta and Ti anomalies, which could be the result of lithospheric subduction affecting magmatic sources (e.g., Kay and Mahlburg-Kay, 1991). The subduction could have culminated with subsequent collision (as rocks show collision features in Figs. 14c and d of Pearce (1996) and Thiéblemont and Tegyey (1994)) and might have provoked the partial melting of crustal materials in the studied area.

7.4.2. Geodynamic implications

The studied rocks are located at the vicinity of the TBF corridor, in the transition zone between the Adamawa-Yade and northern domains. The subduction derived features shown by these rocks could be related to the subduction of an old plate boundary during amalgamation of Gondwana, shown in previous works (e.g., Fozing et al., 2019; Kwékam et al., 2010; Njonfang et al., 2006) along the TBF corridor at the Fomopéa, Kekem and Foumban-Bankim areas. This subduction could be prior to (and/or could have culminated with) continent-continent collision marked by crustal thickening (ca. 630–620 Ma; Ngako et al., 2008) (Fig. 15) as it could be the same tectonic event responsible for the generation of the ca. 660 Ma rocks in the syenitic massif (Yomeun et al., 2022) adjoining the studied rocks. Its manifestations could have locally continued until the interval period (613–585 Ma) of the left lateral wrench movements in Cameroon (Ngako et al., 2008), since the studied rocks crystallized during 603–598 Ma, which is in the same time consistent within error with the late-D_2 regional emplacement in the CAFB (Li et al., 2017; Toteu et al., 2004). This subduction may also indicate an earlier Paleo to Mesoproterozoic event (Nd-T_{DM2} ages at 1188–2120 Ma and zircon Hf-T_{DM2} ages at 2173–2480 Ma) having affected crustal materials slightly mixed locally with an Archean heritage (Nd-T_{DM2} age at 3084 Ma in the orthogneiss YB16) and reactivated during the Pan-African orogeny.

Despite geochemical compositions of igneous rocks reflect the compositions of their source rather than their tectonic setting (e.g., Frost et al., 2001), granitoids sources show significant correlations with tectonic setting (e.g., Pearce, 1996). Therefore, geochemical compositions could be used in certain cases to sustain the tectonic setting. Most of the studied rocks show compositions indicating derivation from the continental crust. However, some of them which plot close or within the mantle-OIB domain in the Ce/Pb versus Ce and Nb/U versus Nb suggest a slight contribution of mantle components in their magmatic sources. The previously reported syenitic massif also shows a slight involvement of mantle material in one of its crustal sources (Yomeun et al., 2022). Therefore, a tectonic model integrating a dominant magmatic accretion along the northern margin of the Congo craton (active margin) associated with subduction, could be considered in the Goa-Mandja area. This subduction could be also related to a possible northwestern subduction-collision system as in the case of the Bape massif (Tchakounté et al., 2021) and Nkondjock area (Kamguia Kamani et al., 2021), respectively at about 150 km and 400 km to the SW of the studied area.

8. Conclusion

(1) U—Pb zircon results show that the Goa-Mandja granitoids, orthogneisses and granitic veins crystallized respectively at 603 ± 3, 602 ± 3 and 598 ± 3 Ma, consistent with the time interval of the left lateral wrench movements and the late-D_2 regional emplacement in the CAFB in Cameroon.

(2) Whole-rock geochemistry, Nd—Sr, zircon O and Lu—Hf isotopes data indicate that the studied granitoids, orthogneisses and granitic veins are dominantly high-K calc-alkaline to shoshonitic and show chemical composition of I-type granitoids. They come from Paleo to Mesoproterozoic crustal materials with reduced to slightly oxidized conditions and locally mixed with Archean heritage and reactivated during the Pan-African orogeny. Their formation could be related to subduction (prior to crustal thickening), which could be an earlier Paleo to Mesoproterozoic event (Nd-T_{DM2} ages at 1188–2120 Ma and zircon Hf-T_{DM} ages at 2173–2480) reactivated during the Pan-African orogeny.

(3) Evidence of Archean crust has not been found in the studied granitoids and granitic vein, thus, they show similarities with some group of juvenile granitoids typical of the North and West Cameroon to the west of the TBF and characterized by calc-alkaline, high-K calk-alkaline to shoshonitic affinities and Nd-T_{DM} ages not older than the Paleoproterozoic. Contrary to granitoids, one Archean Nd-T_{DM2} age has been found among orthogneisses, leading them to conform to some group of rejuvenated granitoids mainly found in the Adamawa-Yade domain characterized by Paleoproterozoic to Archean inheritances. Thus, the Goa-Mandja area belongs to the transitional zone between the Adamawa-Yade and northern domains in Cameroon. It could likely be considered to mark the transition between the northwestern limit of the Congo Craton and the Proterozoic domain.

Declaration of Competing Interest

The authors declare that they have no known competing financial interests or personal relationships that could have appeared to influence the work reported in this paper.

Acknowledgements

This study is part of the ongoing PhD thesis of the first author, at the School of Earth Sciences, China University of Geosciences, Wuhan. It was supported by the National Natural Science Foundation of China (NSFC 41972242) and Fok Ying Tung Education Foundation (171013). We thank Zhaochu Hu for the (MC)-LA-ICPMS analyses, Abing Lin for the whole-rock geochemical analyses, Cai Xinglan for the laboratory assistance, Dr. Lucas Mouafo and Just-Christ Yimgang for their nice supports and advices. The China Scholarship Council (CSC) is deeply appreciated for granting scholarship (2017GXZ015788) to the first author. We are grateful to the administrative and traditional rulers and populations of Linte and its neighborhood villages, Ngambe Tikar, Mamblan, Mandja, Mamboen and Makan localities for their nice support and accommodations during different fieldworks. Constructive comments from two anonymous reviewers and the editor Greg Shellnutt are very helpful and greatly thanked.

Appendix A. Supplementary data

Supplementary data to this article can be found online at https://doi.org/10.1016/j.lithos.2022.106700.

References

Abdelsalam, M.G., Liégeois, J.-P., Stern, R.J., 2002. The Saharan Metacraton. J. Afr. Earth Sci. 34, 119–136.

Ayonta Kenne, P., Tanko Njiosseu, E.L., Ganno, S., Ngnotue, T., Fossi, D.H., Hamdja Ngoniri, A., Nga Essomba, P., Nzenti, J.P., 2021. Zircon trace element geochemistry and Ti in-zircon thermometry of the Linté Pan-African granitoids, Central Cameroon: Constraints on the genesis of host magma and tectonic implications. Geological Journal 1–19.

Azeuda Ndonfack, K.I., Xie, Y., Zhong, R., Yomeun, B.S., Cui, K., Shan, X., 2022. Tectonic evolution of Neoproterozoic rocks, eastern Cameroon: Implication for gold mineralization in the Bétaré Oya and Woumbou-Colomine-Kette districts. Precambrian Research. https://doi.org/10.1016/j.precamres.2021.106475.

Boehnke, P., Watson, E.B., Trail, D., Harrison, T.M., Schmitt, A.K., 2013. Zircon saturation re-revisited. Chem. Geol. 351, 324–334.

Bouvier, A., Vervoort, J.D., Jonathan Patchett, P., 2008. The Lu-Hf and Sm-Nd isotopic composition of CHUR: Constraints from unequilibrated chondrites and implications for the bulk composition of terrestrial planets. Earth Planet. Sci. Lett. 273, 48–57.

Chappell, B.W., White, A.J.R., 1992. I- and S-type granites in the Lachlan Fold Belt. Trans. R. Soc. Edinb. Earth Sci. 83, 1–26.

Chebeu, C., Ngo Nlend, C.D., Nzenti, J.P., Ganno, S., 2011. Neoproterozoic High-K Calc-Alkaline Granitoids from Bapa-Batié, North Equatorial Fold Belt, Central Cameroon: Petrogenesis and Geodynamic significance. The Open Geology Journal 5, 1–20.

Chen, F., Zhu, X., Wang, W., Wang, F., Hieu, P., Siebel, W., 2009. Single-grain detrital muscovite Rb-Sr isotopic composition as an indicator of provenance for the Carboniferous sedimentary rocks in northern Dabie, China. Geochemical Journal 43 (4), 257–273.

Dawaï, D., Bouchez, J.L., Paquette, J.L., Tchameni, R., 2013. The Pan-African quartz-syenite of Guider (North-Cameroon): magnetic fabric and U-Pb dating of a late-orogenic emplacement. Precambrian Res. 236, 132–144.

Djouka-Fonkwé, M.L., Schulz, B., Schüssler, U., Tchouankoué, J.-P., Nzolang, C., 2008. Geochemistry of the Bafoussam Pan-African I- and S-type granitoids in western Cameroon. J. Afr. Earth Sci. 50, 148–167.

Ekwere, S.J., 1985. Li, F and Rb contents and Ba/Rb and Rb/Sr ratios as indicators of postmagmatic alteration and mineralization in the granitic rocks of the Banke and Ririwai Younger Granite complexes, Northern Nigeria. Mineral. Deposita 20, 89–93.

Ferry, J.M., Watson, E.B., 2007. New thermodynamic models and revised calibrations for the Ti-in-zircon and Zr-in-rutile thermometers. Contrib. Mineral. Petrol. 154, 429–437.
Fozing, E.M., Kwékam, M., Gountié Dedzo, M., Asaah Asobo, N.E., Njanko, T., Tcheumenak Kouémo, J., Efon Awouma, J., Njonfang, E., 2019. Petrography and geochemistry of amphibolites from the Fomopéa Pluton (West Cameroon): origin and geodynamic setting. J. Afr. Earth Sci. 154, 181–194.
Frost, B.R., Barnes, C.G., Collins, W.J., Arculus, R.J., Ellis, D.J., Frost, C.D., 2001. A geochemical classification for granitic rocks. J. Petrol. 42, 2033–2048.
Ganwa, A.A., Klötzli, U.S., Diguim Kepnamou, A., Hauzenberger, C., 2018. Multiple Ediacaran tectonometamorphic events in the Adamawa-Yadé Domain of the Central Africa Fold Belt: Insight from the zircon U-Pb LAMICP-MS geochronology of the metadiorite of Meiganga (Central Cameroon). Geol. J. 1–14.
Ganwa, A.A., Klötzli, U.S., Hauzenberger, C., 2016. Evidence for Archean inheritance in the pre-Panafrican crust of Central Cameroon: Insight from zircon internal structure and LA-MC-ICP-MS U-Pb ages. J. Afr. Earth Sci. 120, 12–22.
Ganwa, A.A., Siebel, W., Frisch, W., Shang, C.K., 2011. Geochemistry of magmatic rocks and time constraints on deformational phases and shear zone slip in the Méiganga area, Central Cameroon. Int. Geol. Rev. 33 (7), 759–784.
Griffin, W.L., Pearson, N.J., Belousova, E., Jackson, S.E., van Achterbergh, E., O'Reilly, S. Y., Shee, S.R., 2000. The Hf isotope composition of cratonic mantle: LAM-MC-ICPMS analysis of zircon megacrysts in kimberlites. Geochim. Cosmochim. Acta 64, 133–147.
Harris, N.B.W., Pearce, J.A., Tindle, A.G., 1986. Geochemical characteristics of collisional-zone magmatism. In: Coward, M.P., Reis, A.C. (Eds.), Collision Tectonics, Geological Society, London, Special Publications, vol. 19, pp. 67–81.
Hofmann, A.W., Jochum, K.P., Seufert, M., White, W.M., 1986. Nb and Pb in oceanic basalts: new constraints on mantle evolution. Earth and Planetary Sciences Letters 79, 33–45.
Imeokparia, E.G., 1981. Ba/Rb and Rb/Sr ratios as indicators of magmatic fractionation, postmagmatic alteration and mineralization-Afu Younger Granite complex, Northern Nigeria. Geochem. J. 15, 209–219.
Ishikawa, Y., Sawaguchi, T., Iwaya, S., Horiuchi, M., 1976. Delineation of prospecting targets for Kuroko deposits based on modes of volcanism of underlying dacite and alteration halos. Mining Geology 26, 105–117.
Isseini, M., Andre-Mayer, A.S., Vanderhaegh, O., Barbey, P., Deloule, E., 2012. A-type granites from the Pan-African orogenic belt in southwestern Chad constrained using geochemistry, Sr-Nd isotopes and U-Pb geochronology. Lithos 153, 39–52.
Kamguia Kamani, M.S., Wang, W., Tchouankoue, J.-P., Huang, S.-F., Yomeun, B., Xue, E.-K., Lu, G.-M., 2021. Neoproterozoic syn-collision magmatism in the Nkondjock region at the Northern border of the Congo Craton in Cameroon: Geodynamic implications for the Central African Orogenic belt. Precambrian Res. 353, 106015.
Kanouo, N.S., Kouské, A.P., Lentz, D.R., Yongué, R.F., 2021. New Insights into Neoproterozoic-cretaceous events in the Mamfe Basin (SW Cameroon, Central Africa): evidence from Textural analyses, U-Th Composition, and U-Pb Zircon Geochronology from Granitic Basement. J. Earth Sci. 32, 1472–1484.
Kay, R.W., Mahlburg-Kay, S., 1991. Creation and destruction of lower continental crust. Geol. Rundsch. 80 (2), 259–278.
Kröner, A., Stern, R.J., 2004. Pan-African Orogeny: Encyclopedia of Geology, vol. 1. Elsevier, Amsterdam, pp. 1–12.
Kusky, T.M., Abdelsalam, M., Tucker, R.D., Stern, R.J., 2003. Evolution of the East African and related orogens, and the assembly of Gondwana. Precambrian Res. 123, 81–85.
Kwékam, M., Dunkl, I., Fozing, M.E., Hartmann, G., Njanko, T., Tcheumenak, Kouémo, Njonfang, E., 2020a. Syn-kinematic ferroan high-K I-type granites from Dschang in South-western Cameroon: U-Pb age, geochemistry and implications for crustal growth in the late Pan-African orogeny. Geol. Soc. Lond., Spec. Publ. 502, 19.
Kwékam, M., Liégeois, J.-P., Njonfang, E., Affaton, P., Hartmann, G., Tchoua, F., 2010. Nature, origin and significance of the Fomopéa Pan-African high-K calc-alkaline plutonic complex in the Central African Fold Belt (Cameroon). J. Afr. Earth Sci. 57, 79–95.
Kwékam, M., Talla, V., Fozing, E.M., Tcheumenak Kouémo, J., Dunkl, I., Njonfang, E., 2020b. The Pan-African High-K I-Type Granites from Batié complex, West Cameroon: Age, Origin, and Tectonic Implications. Front. Earth Sci. 8 (363), 1–14.
Lerouge, C., Cocherie, A., Toteu, S.F., Milesi, J.P., Penaye, J., Tchameni, R., Nsifa, N.E., Fanning, C.M., 2006. SHRIMP U-Pb zircon dating for the Nyong Series, South West Cameroon. J. Afr. Earth Sci. 44, 413–427.
Li, X.-H., Chen, Y., Tchouankoue, J.P., Liu, C.-Z., Li, J., Ling, X.-X., Tang, G.-Q., Liu, Y., 2017. Improving geochronological framework of the Pan-African orogeny in Cameroon: New SIMS zircon and monazite U-Pb age constraints. Precambrian Res. 294, 307–321.
Li, X.H., Long, W.G., Li, Q.L., Liu, Y., Zheng, Y.F., Yang, Y.H., Chamberlain, K.R., Wan, D. F., Guo, C.H., Wang, X.C., Tao, H., 2010. Penglai zircon megacrysts: a potential new working reference material for microbeam determination of Hf-O isotopes and U-Pb age. Geostand. Geoanal. Res. 34, 117–134.
Li, X.H., Tang, G.Q., Gong, B., Yang, Y.H., Hou, K.J., Hu, Z.C., Li, Q.L., Liu, Y., Li, W.X., 2013. Qinghu zircon: a working reference for microbeam analysis of U-Pb age and Hf and O isotopes. Geochemistry 58 (36), 4647–4654.
Liew, T.C., Hofmann, A.W., 1988. Precambrian crustal components, plutonic associations, plate environment of the Hercynian Fold Belt Central Europe: Indications from a Nd and Sr isotopic study. Contrib. Mineral. Petrol. 98, 129–138.
Liu, Y.S., Gao, S., Hu, Z.C., Gao, C., Zong, K., Wang, D., 2010. Continental and Oceanic Crust Recycling-induced Melt-Peridotite Interactions in the Trans-North China Orogen: U-Pb Dating, Hf Isotopes and Trace elements in Zircons from Mantle Xenoliths. J. Petrol. 51 (1–2), 537–571.
Loucks, R.R., Fiorentini, M.L., Henriquez, G.J., 2020. New Magmatic Oxybarometer using Trace elements in Zircon. J. Petrol. 1–30.
Ludwig, K.R., 2012. User's manual for Isoplot 3.75. A Geochronological Toolkit for Microsoft Excel. Berkeley Geochronology Center Special Publication 5, 1–75.
Maniar, P.D., Piccoli, P.M., 1989. Tectonic discrimination of granitoids. Geological Society of American Bulletin 101, 635–643.
Middlemost, E.A.K., 1994. Naming materials in the magma/igneous rock system. Earth-Science Review 74, 193–227.
Miller, C.F., McDowell, S.M., Mapes, R.W., 2003. Hot and cold granites? Implications of zircon saturation temperatures and preservation of inheritance. Geology 31, 529–532.
Nardi, L.V.S., Bitencourt, M.D.F., Florisbal, L.M., Ferri, Padilha Dionatan, 2021. Shoshonitic Magmatic Series and the High Ba-Sr Granitoids: a Review with Emphasis on examples from the Neoproterozoic Dom Feliciano Belt of Southern Brazil and Uruguay. J. Earth Sci. 32, 1359–1373.
Ngako, V., Affaton, P., Njonfang, E., 2008. Pan-African tectonics in northwestern Cameroon: Implication for the history of western Gondwana. Gondwana Res. 14, 509–522.
Ngamy Kamwa, A., Tchakounte, J.N., Nkoumbou, C., Owona, S., Tchouankoue, J.-P., Mvondo Ondoa, J., 2019. Petrology and geochemistry of the Yoro-Yangben Pan-African granitoid intrusion in the archaean Adamawa-Yade crust (Sw-Bafia, Cameroon). J. Afr. Earth Sci. 150, 401–414.
Ngo Belnoun, R.N., Tchouankoue, J.P., Itiga, I., Wambo, A.N.S., Owona, S., Koller, F., Thoni, M., 2013. Geochemistry of the Bayon plutonic complex-Western Cameroon. Glob. J. Geol. Sci. 11, 73–93.
Njiekak, G., Dörr, W., Tchouankoue, J.P., Zulauf, G., 2008. U-Pb zircon and microfabrics data of (meta) granitoids of western Cameroun: Constraints on the timing of pluton emplacement and deformation in the Pan-African belt of Central Africa. Lithos 102, 460–477.
Njiosseu, E.L.T., Nzenti, J.P., Njanko, T., Kapajika, B., Nédélec, A., 2005. New U Pb zircon ages from Tonga (Cameroon): coexisting Eburnean-Transamazonian (2.1 Ga) and Pan-African (0.6 Ga) imprints. C. R. Geosci. 337, 551–562.
Njonfang, E., Ngako, V., Kwékam, M., Affaton, P., 2006. Les orthogneiss calco-alcalins de Foumban-Bankim: témoins d'une zone interne de marge active panafricaine en cisaillement. Compt. Rendus Geosci. 338, 606–616.
Pearce, J., 1996. Sources and settings of granitic rocks. Episodes 19 (4), 120–125.
Pearce, J.A., Harris, N.B.W., Tindle, A.G., 1984. Trace elements discrimination diagrams for the geotectonic interpretation of granite rocks. J. Petrol. 25, 956–983.
Peccerillo, A., Taylor, S.R., 1976. Geochemistry of Eocene calc-alkaline volcanic rocks from the Kastamonu area, northern Turkey. Contrib. Mineral. Petrol. 58, 63–81.
Pe-Piper, G., Piper, D.J.W., Koukouvelas, I., Dolansky, L.M., Kokkalas, S., 2009. Postorogenic shoshonitic rocks and their origin by melting underplated basalts: the Miocene of Limnos, Greece. Geol. Soc. Am. Bull. 121, 39–54.
Rapp, R.P., Watson, E.B., 1995. Dehydration melting of metabasalt at 8-32 kbar: implications for continental growth and crust-mantle recycling. J. Petrol. 36, 891–931.
Rudnick, R.L., Fountain, D.M., 1995. Nature and composition of the continental crust: a lower crustal perspective. Rev. Geophys. 33 (3), 267–309.
Rudnick, R.L., Gao, S., 2003. Composition of the continental crust. In: Holland, H.D., Turekian, K.K. (Eds.), The Crust Treatise on Geochemistry 3. Elsevier-Pergamon, Oxford, pp. 1–64.
Shellnutt, J.G., 2021. The enigmatic continental crust of North-Central Africa: Saharan Metacraton or Central Sahara Shield? S. Afr. J. Geol. 124, 383–390.
Shellnutt, J.G., Pham, N.H.T., Denyszyn, S.W., Yeh, M.-W., Lee, T.-Y., 2017. Timing of collisional and post-collisional Pan-African Orogeny silicic magmatism in south-central Chad. Precambrian Res. 301, 113–123.
Shellnutt, J.G., Pham, N.H.T., Yeh, M.-W., Lee, T.-Y., 2020. Two series of Ediacaran collision-related granites in the Guéra Massif, South-Central Chad: tectonomagmatic constraints on the terminal collision of the eastern Central African Orogenic Belt. Precambrian Res. 347, 105823.
Shellnutt, J.G., Yeh, M.-W., Lee, T.-Y., Iizuka, Y., Pham, N.H.T., Yang, C.-C., 2018. The origin of Late Ediacaran post-collisional granites near the Chad Lineament, Saharan Metacraton, South-Central Chad. Lithos 304-307, 450–467.
Shellnutt, J.G., Yeh, M.-W., Pham, N.H.T., Lee, T.-Y., 2019. Cryptic regional magmatism in the southern Saharan Metacraton at 580 Ma. Precambrian Res. 332, 105398.
Shellnutt, J.G., Yeh, M.-W., Pham, N.H.T., Lee, T.-Y., 2021. Late Ediacaran post-collisional magmatism in the Guéra Massif, South-Central Chad. International Geology Review. https://doi.org/10.1080/00206814.2021.1916783.
Silva Filho, A.F., Guimaraes, I.P., Santos, L., Armstrong, R., Van Schmus, W.R., 2016. Geochemistry, U-Pb geochronology, Sm-Nd and O isotopes of ca. 50 Ma long Ediacaran High-K Syn-Collisional Magmatism in the Pernambuco Alagoas Domain, Borborema Province, NE Brazil. J. S. Am. Earth Sci. https://doi.org/10.1016/j.jsames.2015.12.013.
Sláma, J., Kosler, J., Condon, D., Crowley, J., Gerdes, A., Hanchar, J., Horstwood, M., Morris, G., Nasdala, L., Norberg, N., 2008. Plesovice zircon-a new natural reference material for U-Pb and Hf isotopic microanalysis. Chem. Geol. 249 (1–2), 1–35.
Söderlund, U., Patchett, P.J., Vervoort, J.D., Isachsen, C.E., 2004. The 176 Lu decay constant determined by Lu-Hf and U-Pb isotope systematics of Precambrian mafic intrusions. Earth Planet. Sci. Lett. 219, 311–324.
Sun, S.S., McDonough, W.F., 1989. Chemical and isotopic systematics of oceanic basalts: Implication for mantle composition and processes. In: Saunder, A.D., Norry, M.J. (Eds.), Magmatism in the Ocean Basins. Geological Society, London, Special Publications, vol. 42, pp. 313–345.
Tagne-Kamga, G., 2003. Petrogenesis of Neoproterozoic Ngondo plutonic complex (Cameroon West Central Africa): a case of late collisional ferro-potassic magmatism. J. Afr. Earth Sci. 36, 149–171.

Tchakounté, J., Eglinger, A., Toteu, S.F., Zeh, C., Nkoumbou, C., Mvondo Ondoa, J., Penaye, J., De Wit, M., Barbey, P., 2017. The Adamawa-Yadé domain, a piece of Archaean crust in the Neoproterozoic Central African Orogenic belt (Bafia area, Cameroon). Precambrian Res. 299, 210–229.

Tchakounté, J.N., Fuh, C.G., Ngamy Kamwa, A., Metang, V., Mvondo Ondoa, J., Nkoumbou, C., 2021. Petrology and geochemistry of the Pan-African high-K calc-alkaline to shoshonitic-adakitic Bapé plutonic suites (Adamawa-Yade block, Cameroon): evidence of a hot oceanic crust subduction. Int. J. Earth Sci. https://doi.org/10.1007/s00531-021-02060-6.

Tchameni, R., Pouclet, A., Penaye, J., Ganwa, A.A., Toteu, S.F., 2006. Petrography and geochemistry of the Ngaoundéré Pan-African granitoids in Central North Cameroon: Implications for sources and geological setting. J. Afr. Earth Sci. 44, 511–529.

Tchouankoue, J.P., Li, X.-H., Ngo Belnoun, R.N., Mouafo, L., Pinto Ferreira, V., 2016. Timing and tectonic implications of the Pan-African Bangangte syenomonzonite, West Cameroon: Constraints from in-situ zircon U-Pb age and Hf-O isotopes. J. Afr. Earth Sci. 124, 94–103.

Thiéblemont, D., Tegyey, M., 1994. Une discrimination géochimique des roches différenciées témoin de la diversité d'origine et de situation tectonique des magmas calco-alcalins. Comptes Rendus Académie des Sciences, Paris 319, 87–94.

Toledo, B.B., de Assis Janasi, V., 2021. Petrogenesis of Granites from the Ediacaran Socorro Batholith, SE Brazil: Constraints from Zircon Dating, Geochemistry and Sr-Nd-Hf Isotopes. J. Earth Sci. 32, 1397–1414.

Toteu, S.F., Penaye, J., Deloule, E., Van Schmus, W.R., Tchameni, R., 2006b. Diachronous evolution of volcano-sedimentary basins north of the Congo craton: Insights from U-Pb ion microprobe dating of zircons from the Poli Lom and Yaoundé Groups (Cameroon). J. Afr. Earth Sci. 44, 428–442.

Toteu, S.F., Penaye, J., Poudjom Djomani, Y.H., 2004. Geodynamic evolution of the Pan-African belt in Central Africa with special reference to Cameroon. Can. J. Earth Sci. 41, 73–85.

Toteu, S.F., Yongue Fouateu, R., Penaye, J., Tchakounté, J., Seme Mouangue, A.C., Van Schmus, W.R., Deloule, E., Stendal, H., 2006a. U-Pb dating of plutonic rocks involved in the nappe tectonic in southern Cameroon: consequence for the Pan-African orogenic evolution of the central African fold belt. J. Afr. Earth Sci. 44, 479–493.

Touret, J.L.R., Huizenga, J.M., 2012. Charnockite microstructures: from magmatic to Metamorphic. Geosci. Front. 3, 745–753.

Trail, D., Watson, E.B., Tailby, N.D., 2012. Ce and Eu anomales in zircon as proxies for oxidation state of magmas. Geochim. Cosmochim. Acta 97, 70–87.

Valley, J.W., Chiarenzelli, J.R., McLelland, J.M., 1994. Oxygen isotope geochemistry of zircon. Earth Planetary Sciences Letters 126, 187–206.

Van Schmus, W.R., Oliveira, E.P., Da Silva Filho, A.F., Toteu, S.F., Penaye, J., Guimaraes, I.P., 2008. Proterozoic links between the Borborema Province, NE Brazil, and the Central African Fold Belt. Geol. Soc. Lond., Spec. Publ. 294, 69–99.

Wang, W., Cawood, P.A., Zhou, M.F., Pandit, M.K., Xia, X.P., Zhao, J.H., 2017. Low-δ18Orhyolites from the Malani Igneous Suite: a positive test for South China and NW India linkage in Rodinia. Geophys. Res. Lett. 44, 10298–10305.

Wang, W., Pandit, M.K., Zhao, J.-H., Chen, W.-T., Zheng, J.-P., 2018. Slab break-off triggered lithosphere - asthenosphere interaction at a convergent margin: the Neoproterozoic bimodal magmatism in NW India. Lithos 296-299, 281–296.

Wang, W., Cawood, P.A., Pandit, M.K., Zheng, J.P., Zhao, J.H., 2019. No collision between Eastern and Western Gondwana at their northern extent. Geology 474, 308–312.

Weecksteen, G., 1957. Carte géologique de reconnaissance à l'échelle de 1/500.000, feuille Douala-Est avec Notice explicative. Direction des Mines et de la Géologie, Yaoundé, Imprimerie Nationale, Cameroun 69.

Yang, Q., Xia, X., Zhang, W., Zhang, Y., Xiong, B., Xu, Y., Wang, Q., Wei, G., 2018. An evaluation of precision and accuracy of SIMS oxygen isotope analysis. Solid Earth Sciences 3, 81–86.

Yomeun, B.S., Wang, W., Kamguia Kamani, M.S., Tchouankoue, J.P., Jiang, Y.-D., Huang, S.F., Azeuda Ndonfack, K.I., Xue, E.K., Lu, G.M., Basua, E.A.A., 2022. Geochronology, geochemistry and Sr-Nd, Hf-O isotope systematics of the Linte massif, Adamawa - Yade domain, Cameroon: implications on the evolution of the Central African Fold Belt. Precambrian Research, 106675. https://doi.org/10.1016/j.precamres.2022.106675. In press.

Zhu, J.J., Richards, J.P., Rees, C., Creaser, R., DuFrane, S.A., Locock, A., Petrus, J.A., Lang, J., 2018. Elevated Magmatic Sulfur and Chlorine Contents in Ore-Forming Magmas at the Red Chris Porphyry Cu-au Deposit, Northern British Columbia, Canada. Econ. Geol. 113, 1047–1075.